UNIVERSITY OF CALIFORNIA
RIVERSIDE

Modeling and Characterization of Ultraviolet Scattering Communication Channels

A Dissertation submitted in partial satisfaction
of the requirements for the degree of

Doctor of Philosophy

in

Electrical Engineering

by

Haipeng Ding

August 2011

Dissertation Committee:

Professor Zhengyuan Xu , Chairperson
Professor Yingbo Hua
Professor Albert Wang

The Dissertation of Haipeng Ding is approved:

Committee Chairperson

University of California, Riverside

Acknowledgments

I am deeply grateful to my advisor, Dr. Zhengyuan Xu. Dr. Xu has been more than an advisor to me. He has guided me through my Ph.D. research by teaching me scientific thinking methods, sharing his enthusiasm and knowledge with me. I would like to sincerely thank Dr. Xu for his long-term help and support for everyday research and life. I would also like to thank the Department of Electrical Engineering at UC Riverside, especially the members of my doctoral committee, Professor Yingbo Hua and Professor Albert Wang, for their valuable support.

My research was benefited from insightful discussion with Dr. Gang Chen in our lab. Dr Chen set up the experimental test systems. We collaborated to conduct extensive measurements, which provided invaluable input to my dissertation and I appreciate his academic help and friendship.

I had the pleasure of working closely with team members in Dr. Xu's lab. I am grateful to the friendship of all members of the research group: Qunfeng He, Ning Liu, Leijie Wang, Yiyang Li, Kaiyun Cui, Zongyu Dong, and Bo Bai.

My research and life at UC Riverside have been enriched by my best friends, Xuechen Chen, Guanxiong Liu, Shengyang Xu, He Tang, Yang Gao, and Yu Sun. I especially thank He Tang for his continuous encouragement to work out together in gym. I would also thank all the badminton friends at UCR for skill training and games.

Finally, and most importantly, none of this would have happened without the love of my family. I would like to give my best gratitude to my parents. Their support, encouragement and love always help me through every phase of my life. My parents work hard and provide me a model for me to focus on my research. I thank Tienhuei. I could never have done this without her support and love. She has truly encouraged

and helped me when difficulties are encountered. Without my family's endless love, this research work would not happen. My dissertation is dedicated to them.

To my family.

ABSTRACT OF THE DISSERTATION

Modeling and Characterization of Ultraviolet Scattering Communication Channels

by

Haipeng Ding

Doctor of Philosophy, Graduate Program in Electrical Engineering
University of California, Riverside, August 2011
Professor Zhengyuan Xu , Chairperson

This thesis studies modeling of non-line-of-sight (NLOS) ultraviolet (UV) scattering channels and the corresponding communication link performance. The research focuses on the channel impulse response and path loss models based on extensive field measurements and theoretical characterization. In NLOS UV scattering environments, transmitted signals suffer from severe atmospheric attenuation and fading before arriving at a receiver, such as absorption, scattering, and turbulence. The thesis is devoted to development of analytical and experimental models to characterize NLOS UV communication channels.

The author conducts comprehensive channel measurements for short communication ranges up to a few hundred meters and proposes an empirical path loss model. Meanwhile, an algorithm is developed to simulate the NLOS UV channel impulse response and path loss based on photons stochastic migration in the atmosphere. Effects of atmosphere conditions on single scattering and multiple scattering are investigated. An empirical curve-fitting model is developed to simplify the modeling work. Monte Carlo simulations provide good channel prediction for field tests in many scenarios. Then short range communication link performance is studied based on the theoretical

models, and limitations by power and channel bandwidth are examined. Link budget results are also extended to long range communication links up to 5 kilometers. In this case, atmosphere turbulence becomes pronounced, and thus the intensity fluctuation at the receiver is mathematically modeled. These modeling results can provide insight into the performance tradeoffs and algorithm design for practical NLOS UV communication systems.

Contents

List of Figures

List of Tables

Chapter 1

Introduction

1.1 History of Wireless Optical Communication

In the past decades, increasing attention and efforts have been placed on wireless optical communication systems [1]-[2]. A wireless optical communication system employs an optical wave with wavelength ranging from infrared, visible light to ultraviolet (UV) to convey information. Compared with a radio frequency (RF) system, it demonstrates several potential advantages [1], such as huge unlicensed bandwidth, low-power and miniaturized transceiver, higher power densities, high resistance to jamming, and potential increase of data rate. In the wireless optics domain, infrared and UV waves are very valuable carriers and have been extensively researched and developed since 1960s [3]-[4].

Similar to a RF link, a typical wireless optical communication link consists of an information source, modulator, transmitter, propagation channel, and receiver [1]. To generate an optical source, light-emitting diodes (LEDs), solid state laser and laser diodes (LD) can be used [5]. An LED radiates light energy from interaction of semiconductor junctions excited by external current. The junction characteristics

determine the emitted wavelength. It usually produces a low-power (up to tens of milli-watts) and less-focused beam. A laser uses gain medium to fill an optical cavity between mirrored facets and radiates amplified light with more focused high power (watts), but it is much bulkier. An LD uses a semiconductor junction to reinforce the field between substrates. Hence it combines properties from the former two devices, i.e., higher power (tens of mWs) and better focus.

For communication purposes, information signals are applied to modulate the light source. Intensity modulation, on-off keying (OOK) and pulse position modulation (PPM) are widely used modulation schemes. If modulated light is emitted from a source and propagates through an atmospheric channel, then various adverse effects of atmospheric constituents will occur [6],[7]. Turbulence induces random fluctuations in the atmosphere's temperature and pressure, resulting in random irregularities. Although it may generate wavefront distortions for longer propagation path, its detrimental effects are not as significant as absorption and scattering from molecules and aerosols such as haze, fogs, clouds, and rain. Molecular species cause wave scattering [8]. Scattering can be described by Rayleigh's fourth power law (scattered signal strength is inversely proportional to λ^4 for wavelength λ), which is a limiting case of the Mie's solution (gaseous molecule radius $r << \lambda$). Absorption is caused by interaction of waves with the constituents. During propagation, transmitted photons undergo single or multiple scattering and absorption by the medium. Those processes cause large angle of arrival (AOA) dispersion, wider beam spreading, reduced spatial coherence, and large multipath spreading. Thus a receiver with adjustable field-of-view (FOV) is usually desirable. The size of aerosols typically ranges in radius between 10^{-3} μm and 10^2 μm, equivalently covering the typical optical spectrum [6].

An optical receiver is composed of a lens-focusing and filtering subsystem,

photodetector and postdetection processor. Optical lens and filters choose particular wavelength-sensitive materials to extract the desired optical field. The photodetector is made of photosensitive materials and produces free electrons with incident photons [1]. Electrons move from a vacuum cavity to a charged anode plate for a vacuum tube or in a positive-negative (PN) junction for a solid-state detector. A current flow is formed by directional shift of those electrons driven by an external electrical potential. A large current can be achieved by a photomultiplication process that makes the excited electrons regenerate additional ones, and produce secondary electron emissions in a vacuum tube or avalanching effect in a solid-state detector. Electric current can then be converted to a voltage for post processing when passing through a load resistor or a more complicated circuit. For a practical photodector, other parameters also affect the quality of the detector output signal such as quantum efficiency and dark current. Phototube and solid-state devices are basic practical photodectors. A photomultiplier tube (PMT) is a phototube with multiple dynodes. Silicon or germanium materials determine the sensitivity to different wavelengths. A photodiode is a solid-state PN junction device called a PIN diode. The gap material is responsive to the wavelength. PIN diodes have small collecting areas, moderate dark current and extremely high bandwidth. The avalanche photodiode (APD) is a solid-state diode using repeated electron ionization, generating a reasonably high multiplier gain. In direct (noncoherent) detection, information is intensity modulated onto the emitted light source. A photodetector outputs a shot noise process whose count rate is proportional to the instantaneous received power. Intensity variation of the transmitted field is thus reflected by the power change. The postdetection processor intends to recover transmitted information from converted current, similar to a standard RF decoding. This process may vary depending on the tradeoff between complexity and performance, such as employing diversity techniques, maximum

likelihood sequence detection (MLSD) [9], and simplified suboptimal methods [10]. It is believed that more sophisticated signal processing techniques will bring significant performance gains in some applications.

1.2 Motivation and Progress of NLOS UV Communication

As a medium for short-range indoor communication, infrared radiation has shown significant advantages over RF [11], [12]. Despite that infrared can use low power sources such as LEDs and in a line-of-sight (LOS) or diffusion scenario, there are some application scenarios where an infrared link is vulnerable to blockage due to little reflection. In addition, the outdoor solar background and indoor florescent light noise, as well as receiver's dark noise, would greatly limit infrared communication performance. As an alternative, NLOS UV communication technology shows significant potential for relaxing the stringent requirements for pointing, acquisition, and tracking (PAT) due to characteristics of UV waves and their unique interactions with atmosphere medium.

First, UV-C (200∼280 nm) or termed deep UV spectrum is solar blind [13]. The solar radiation observed outside the atmosphere has a wavelength-dependent energy distribution due to the constituents of the sun. Only about 9% is responsible for the UV where only about less than 1% is in the UV-C. To reach the Earth's surface, that solar radiation must traverse Earth's atmosphere and loses energy by absorption and scattering. The relatively high transmission occurs for the longer wavelengths, and much stronger absorption is observed for the UV. The attenuation becomes appreciable and increases rapidly toward shorter wavelengths [14]. Larger attenuation together with strong absorption of ozone in the upper atmosphere makes solar radiation in the UV-C region to be negligible. By operating in this region, a ground-based photodetector can

exploit the low background radiation to approach quantum-limited photon-counting detection. This characteristic encourages development of wide FOV receivers to greatly increase received energy without much enhancement of background noise. Second, due to short wavelength of UV waves, high degree of relatively angle-independent scattering occurs when UV waves transverse the atmosphere full of molecular and aerosols, creating tremendous communication paths from the source to the destination. Consequently, NLOS communication is enabled. It thus relaxes stringent PAT requirements at the receiver. This property is critical for communications when LOS is not possible. Third, due to high attenuation by the atmosphere, signal beyond the extinction range (usually a few kilometers) can hardly be intercepted, a desirable feature for tactical applications. Finally, huge and unlicensed spectrum in the UV band may potentially deliver high data rate services, a few times higher than the infrared counterpart. For conditions in which low-power consumption, low-cost implementation, NLOS operability and security are essential, while range and bandwidth requirements are modest, the UV technology is ideal. It may find diverse applications in data communication, surveillance sensor networks, homeland security, unattended ground sensor (UGS) networks, and small unit communications in urban terrain environments [15]. It is also promising for communications between unmanned aerial vehicles (UAVs) and attended terminals, or for detection of chemical and biological agents. Certainly, the UV technology is also suitable for LOS channels.

Very importantly, for eye and skin safety, the International Commission on Non-Ionizing Radiation Protection (ICNIRP) and the International Electrotechnical Commission (IEC) enforce UV exposure power limits [16]. In the deep UV region, the minimum allowable continuous exposure limit occurs at wavelength of 270 nm at a level as low as 3 mJ per cm^2 per second, while increasing to 100 mJ at 200 nm and

3.4 mJ at 280 nm. Those limits proportionally decrease with exposure time in seconds. So UV related communication system design and experimentation should follow these safety rules.

Research interests in NLOS UV communications can be divided into two types. The first is the investigation of channel characteristics by analysis, experimentation, and simulation. The second is the development of communication technologies such as system transceiver design and modulation study. While modulation and transceiver design are key elements for a successful NLOS UV optical communication system, the communication channel represents a critical component for link and system performance evaluation. From NLOS UV channel impulse response, one can easily obtain key system performance parameters, including channel temporal spread, path loss and channel bandwidth, which will correspondingly provide guidelines to system design. A considerable volume of work has been done to characterize communication channel responses of general optical links. However, because NLOS optical systems operate at an indirect link path with complex system factors such as atmosphere conditions and complicated link geometries, comprehensive understanding of the channel characteristics is required to achieve the performance potentials of practical NLOS optical communication links.

Study on NLOS UV communications started decades ago, dating back to 1960's. A pioneering experimental work focused on scatter UV link characterization [3]. It used a xenon flashtube as a UV source to radiate waves of continuous spectrum with shortest wavelength of 280 nm at high power. The PMT based receiver was separated from the transmitter by a 26 km range, resulting in an equivalent NLOS propagation path of 40 km under the experimental path geometry. Performance of tested NLOS link was calculated. Afterwards, a pioneering analytical work developed an elegant theoretical channel response model to describe the temporal characteristics of scattered radiation

in the middle UV of 200∼300 nm [8]. The model was built upon a prolate spheroidal coordinate system under an assumption that each photon underwent single interaction with constituents in the transmitter/receiver overlapped cone volume. Different types of scattering events could be incorporated and described by phase functions. It was shown that total scattering from molecular and aerosol predominates at long wavelength while absorption at short wavelength. The model was further extended to examine angular spectra and path losses [17],[18]. Meanwhile, a NLOS UV system based on an isotropic radiating mercury arc lamp at modulation rate of 40 kHz was also demonstrated [19], and later an improved UV local area network test-bed spanning a kilometer range based on a collimated mercury-xenon lamp was built to increase modulation rate up to 400 kHz at effective wavelength 265 nm [20]. A UV laser communication system at 266 nm that radiated short pulses at high peak power was also reported [21]. However, the modulation rate was only 600 Hz.

The early UV NLOS systems were limited to employing rather bulky, power hungry, bandwidth-limited flashtube/lamp/laser UV sources. Semiconductor UV optical sources offer the potential of low cost, small size, low power, high reliability, and high bandwidth. State-of-the-art device technology has enabled miniaturized UV LEDs, for example as reported in [22] and [23]. Those LEDs are no bigger than one square millimeter, offer a series of wavelengths in the deep UV region, typically consume electrical power of 150 mW and radiate optical power of 0.5 mW. Consequently, the arrival of this new generation of UV sources has inspired new studies of LED-based UV systems, with applications in sensing and short range communications.

Shaw et.al. [24]-[25] reported on experiments using a 24-element LED array at 274 nm, producing 40 mW optical power. They used a relatively large transmit divergence angle of about 50^o. A NLOS link was configured by setting transmitter (Tx) and

receiver (Rx) pointing angles equal to 90^o (vertical pointing). At the receiver, a Perkin Elmer PMT (MP-1921) was combined with a solar blind filter to achieve an overall rejection ratio exceeding 10^{10} in the visible through infrared bands. The system was shown to reliably deliver a data rate of 2.4 kbps using 4-PPM with transmitter and receiver separation of 11 m (or 200 bps at 100 m). Iterative and Monte Carlo methods have been studied by French researchers for the calculation of the aureole about a point source due to atmosphere scattering in the middle ultraviolet [26]. A NLOS optical wireless sensor network based on UV multiple backscattering was introduced in [27]. A mathematical model for the optical received signal power was developed using the bistatic lidar equation approach. The model was then applied to evaluate the viability and limitations of the inter-node link, and predict the communication performance. Their analysis is valuable for design and study of miniature operational sensor networks. Recently, [28]-[29] developed new NLOS UV path loss and impulse response measurement systems and conducted significant field tests for both modeling and system design.

To gain a clear vision of NLOS optical channels, we propose a comprehensive procedure for channel characterization. We carry out experimental channel measurements, computer simulations, and also analytical studies for NLOS UV channel models based on multiple scattering assumptions from the radiative transfer theory. We aim to achieve a thorough understanding of NLOS channel characteristics that will offer both accuracy and generality.

1.3 Contributions and Outline of the Thesis

Multiple scattering modeling and experimental characterization of the NLOS UV scattering channel have received little attention in the literature. Multiple scat-

terings may contribute dominantly in specific scenarios for the atmospheric NLOS UV communication system. And complete field measurements will further validate existing theory and models. This dissertation addresses NLOS UV multiple scatterings by developing algorithms that can be used to track the photon's interactions with atmosphere. NLOS UV channel measurement systems are set up to conduct comprehensive field tests and obtain complete channel sounding results for varying geometries. The theories and measurements are compared against each other, from which important conclusions on channel characteristics and communication link performance are drawn. The procedure is effective for traditional wireless optical channels as well.

Preliminary work at University of California, Riverside has shown that NLOS UV scattering communications are unique and can be quite different from their infrared counterparts. Xu et.al analyzes the approximated performance of wireless UV links and presents the key link components for the NLOS UV scattering communications in outdoor environments. This dissertation extends previous work in three important ways. Firstly, two measurement (impulse response and path loss) systems illustrate that the NLOS UV channel is geometry and atmosphere dependent. Secondly, UV channel impulse response and path loss are theoretically derived and analyzed by considering multiple scatterings. Thirdly, NLOS UV turbulence is modeled and scintillation effect on a NLOS UV channel is studied.

The remaining four chapters of this dissertation are summarized as follows:

Chapter 2 introduces the free space atmosphere channel, mainly focusing on the optical properties of the atmosphere. NLOS UV related Rayleigh and Mie scattering are briefly reviewed. Typical scattering, absorption and extinction coefficients are tabulated. Regarding the NLOS UV scattering channel, the author uses a composite scattering phase function for analysis and modeling, and also analyzes the existing methodology

for channel modeling.

In Chapter 3, the author develops the extensive field test methods for the short range NLOS UV channel. Specifically, our UV measurement systems are introduced in detail. Path loss results for ranges up to 100 meters are obtained and analyzed. An empirical path loss model is derived and validated. NLOS UV channel impulse response measurements are also conducted and further validated by simulations in Chapter 4.

Chapter 4 develops theoretical NLOS UV models and study UV communication link performance. Case studies demonstrate the significance of multiple scattering in specific atmosphere conditions. The numerical examples show that NLOS UV communications are geometry and atmosphere dependent. Applying the modeling results, the author also reveals the tradeoff between UV channel bandwidth and transmitted power. Combining scattering and LOS turbulence analysis, the author also derives a received signal distribution model for the NLOS UV turbulence channel.

Chapter 5 highlights the contents of the dissertation and the major results.

Chapter 2

Fundamentals of NLOS UV Communication Systems

UV communication systems are suitable for both commercial and military applications. Due to the property of solar blindness, UV systems are immune to both natural and artificial electromagnetic interference. Strong scatterings further make NLOS communication powerful in counteracting the spatial shadowing and blocking effects. The UV transceivers also have the capability to be covert from being detected and eavesdropped.

2.1 NLOS UV Communication Systems

UV communication systems consist of UV sources, atmosphere channel and UV detectors. Data signals are encoded and modulated to UV carriers, and UV sources will emit the modulated UV signals into the atmosphere. UV signals will experience molecular and particular scattering and absorption. Although most of the UV signals will be scattered and absorbed by the atmosphere, sufficient scatterings will bring UV

signals into the FOV of a UV detector. To improve the signal to noise ratio, UV filters are used to suppress the out-of-band background noise. The received signal is then transformed back into the electric signal to complete the information exchange between transmitter and receiver in the communication system.

2.1.1 UV Sources

Previously, researchers used UV flashtube/lamp/lasers as sources. These devices are typically bulky, power hungry, or bandwidth limited. Semiconductor UV optical sources offer the potential of low cost, small size, low power, high reliability, and high bandwidth. State-of-the-art development by the Sensor Electronic Technology (SET) Corporation has produced commercialized deep UV LEDs (UVTOP series). This work was sponsored as part of the Defense Advanced Research Projects Agency (DARPA) Semiconductor UV Optical Source (SUVOS) program to develop semiconductor UV emitters. SET offers UV LEDs with minimum peak wavelengths from 250 nm to 355 nm at a step of 5 nm with accuracy of $\pm$10 nm. There are flat window, hemispherical lens and ball lens packaging types, yielding different divergent angles. The actual product may show variable offsets from specifications. Each LED is characterized by power-current, power distribution over wavelength and angle, duty cycle, life time, peak and average power, and minimum pulse width. Figure 2.1 shows measured output optical power for different driving currents under continuous operations. The average power of 0.3 mW and 0.37 mW is delivered at driving current 30 mA for two different LEDs. In a reliable operation mode without cooling, using pulse width of 50 ns and duty cycle of 1:100, the forward current for UVTOP280 can be as large as 200 mA, yielding stable average power of 6 mW. Increasing the duty cycle, the average power approximately proportionally increases before reaching the upper limit on the duty cycle, saying 1:25.

On this basis, the peak power is calculated about 6 mW with a large current. On the other hand, the driving current can vary, with the maximum going beyond 1 A for pulsed operation at a low duty cycle. Accordingly, the peak power can significantly increase to more than 12 mW. The full-width half-maximum (FWHM) bandwidth of UVTOP280 is found to be 10 nm, a similar level was found for UVTOP250. The minimum pulse width is 20 ns that yields a maximum bandwidth of 50 MHz. The beam angular distribution is found to follow a Gaussian shape, whose standard deviation is about 5^o, yielding a divergence angle of $\pm 5^o$.

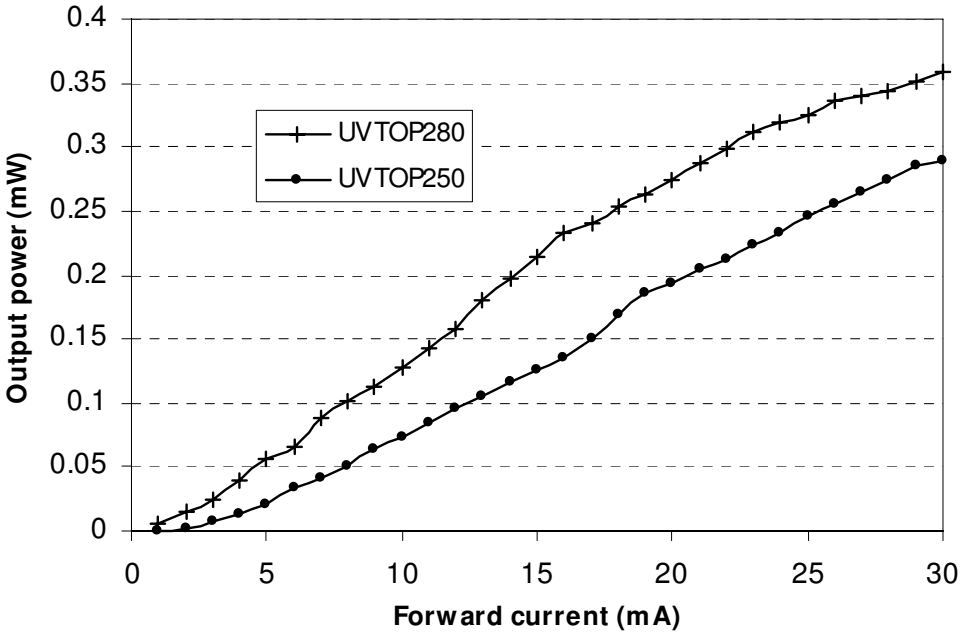

Figure 2.1: Measured output power of UV LEDs for different forward currents.

For the UV source, there is no commercial laser diode in the solar blind band. UV LEDs typically deliver low optical power, with LED arrays up to 50 mW. Limited power level will constrain the communication distance between the transmitter and receiver. Consequently, UV laser is an option to provide high power for long range communication links. In our measurement system, we employed a Q-switched solid

state UV laser for long range channel measurement. The transmitter was a compact Q-switched fourth harmonic Nd:YAG laser at 266 nm triggered by a rectangular pulse at 10 Hz from a signal generator, producing a corresponding laser pulse train at 10 Hz. Each pulse had width of (3-5) ns and energy up to (3-5) mJ, and can be attenuated manually by a factor of 10^3 with an integrated attenuator. A drawback is that the laser could not be modulated at continuously varying frequencies.

2.1.2 UV Filter and Detector

UV filter and UV detector are important elements for UV communication systems. Generally, solar blind filters and UV PMTs are developed and employed in recent UV communication systems. Taking our measurement system as an example, two UV PMTS, Perkin Elmer MP1922 and Hamamatsu R7154, are considered. Both are solar blind. MP1922 has a built-in current preamplifier and a head-on type PMT with a circle sensing window with a diameter of 1.5 cm (resulting in an active area of $1.77cm^2$). It has a spectral response from 165 nm to 320 nm, 10 dark counts per second. The peak quantum efficiency of 15% and peak gain of 10^6 occurs at 200 nm, while decreasing quickly towards longer wavelengths, about 10% at 260 nm and 7% at 280 nm. R7154 is a side-on type PMT with a rectangular window size 0.8 cm $\times$ 2.4 cm which is $1.92cm^2$. It has peak sensitivity at 254 nm over its spectral response from 160 nm to 320 nm. The maximum quantum efficiency reaches 30%, and high gain of 10^7. It has a similar pulse rise time of a few nanoseconds, while the electron transit time of 22 ns. The inherent bandwidth is thus about 40 MHz. However, its dark current is much larger, showing at least three times higher in the Equivalent Noise Input. Two solar blind filters centered at 255 nm and 271 nm are used. Their FWHM is 15 nm. The in-band peak transmission is up to 10%, and out-of-band peak transmissions are 10^{-10} from 300 nm to 770 nm, and

2×10^{-4} from 770 nm to 1100 nm. Combined with UV enhanced PMTs, the out-of-band rejection ratio of about 10^8 is typically achievable for the band of interest.

2.2 UV Atmosphere Channel

2.2.1 The Communication Medium: Atmosphere

The atmosphere can be viewed as a complex composition of molecules and aerosols, such as gases, water vapor, pollutants, and other chemical particles. These atmospheric particles interact with the radiation fields generated by an emitter, and cause the signal power losses and wavefront distortion. These interactions are generally classified as scattering and absorption. From a photon propagation point of view, scattering implies a redirection of the angle of propagation, whereas absorption means the photon is annihilated. The magnitude of the atmospheric interaction varies considerably with meteorological conditions, generally becoming stronger as the optical wavelength approaches the cross-sectional dimension of the atmospheric particles (which explains the strong scattering observed in the UV spectrum). Scattering is generally modeled through Rayleigh and Mie theory, as a function of the wavelength and particle size, e.g., [30]. Both of these are included in the models described in the following. Scattering enables NLOS communications, although the great majority of photons are either absorbed or scattered away from the intended detector yielding large path loss.

Atmospheric turbulence due to random non-homogeneity in the atmosphere will cause local changes in the refractive index [30], that induces distortion in the optical wavefront. This effect is well known in coherent line-of-sight (LOS) laser communications, where a distorted wavefront arriving at the detector can limit communications rates or received signal quality. Here, we first consider NLOS communications due to

scattering over relatively short range, and ignore turbulence effects. Turbulence analysis for NLOS UV will be postponed to Chapter 4. We consider coherent scattering, where energy lost from the primary field is redistributed to a scatter field which has the same wavelength as the primary. Absorption considers all other interactions (true absorption, incoherent scattering, etc.) in which "absorbed"energy is lost to the total radiation field (primary and coherently scattered radiation).

2.2.2 The NLOS UV Scattering Channel

The NLOS UV channel involves both molecular scattering and absorption, and aerosol scattering and absorption. We first ignore atmospheric turbulence and focus on relatively short-range propagation where turbulence typically plays a very small role. For NLOS UV communications, scattering serves as the vehicle for information exchange between the transmitter and receiver. The scattered light that reaches the receiver depends on the link geometry and the optical properties of the atmosphere, as described next.

Consider a typical NLOS communication geometry illustrated by [17] and [4], as shown in Figure 2.2. Denote the Tx beam full-width divergence angle by ϕ_1, the Rx FOV angle by ϕ_2, the Tx apex angle by θ_1, Rx apex angle by θ_2, the Tx and Rx baseline separation by r, and the distances of the intersected (overlap) volume V to the Tx and Rx by r_1 and r_2, respectively.

From the communications viewpoint, scattering and absorption are the two dominant types of photon interactions with the atmosphere over a short communication range. We assume a homogeneous atmosphere and use the following coefficients: the Rayleigh (molecular) scattering coefficient k_s^{Ray}, Mie (aerosol) scattering coefficient

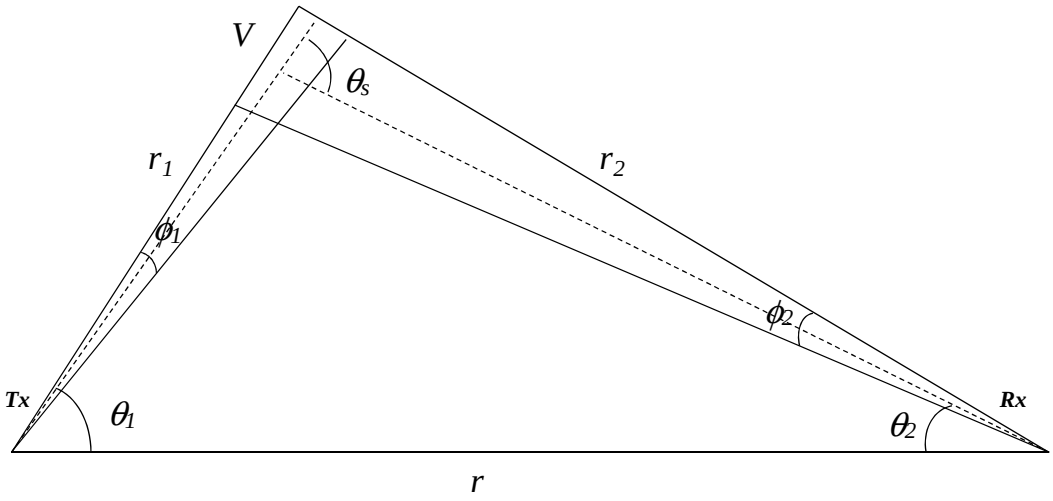

Figure 2.2: NLOS UV communication link geometry, depicting elevated transmitter beam and receiver field-of-view.

Table 2.1: Atmosphere model parameters: 230-310 nm

λ(nm)	k_s^{Ray}(km^{-1})	k_s^{Mie}(km^{-1})	k_a(km^{-1})
230	0.493	0.623	2.581
240	0.406	0.531	1.731
250	0.338	0.421	1.202
260	0.266	0.284	0.802
270	0.241	0.277	0.621
280	0.194	0.272	0.322
290	0.177	0.266	0.046
300	0.145	0.261	0.039
310	0.132	0.234	0.005

k_s^{Mie}, absorption coefficient k_a, and extinction coefficient k_e. The total scattering coefficient is defined as the sum of the two scattering coefficients $k_s = k_s^{Ray} + k_s^{Mie}$, and the extinction coefficient is given by the sum of the scattering and absorption coefficients as $k_e = k_s + k_a$. We consider gas concentration and optical features of the atmosphere in Table I from Table II in [31] for middle UV radiation.

The scattering phase function is modeled as a combination of Rayleigh and Mie scattering phase functions based on the corresponding scattering coefficients, as

suggested by [32]

$$P(\mu) = \frac{k_s^{Ray}}{k_s} p^{Ray}(\mu) + \frac{k_s^{Mie}}{k_s} p^{Mie}(\mu), \tag{2.1}$$

where $\mu = \cos\theta_s$ is defined from the scattering angle θ_s. The two phase functions follow a generalized Rayleigh model and a generalized Henyey-Greenstein function, respectively, given by

$$p^{Ray}(\mu) = \frac{3[1 + 3\gamma + (1-\gamma)\mu^2]}{16\pi(1+2\gamma)}, \tag{2.2}$$

$$p^{Mie}(\mu) = \frac{1-g^2}{4\pi}[\frac{1}{(1+g^2-2g\mu)^{3/2}} + f\frac{0.5(3\mu^2-1)}{(1+g^2)^{3/2}}], \tag{2.3}$$

where γ, g, and f are model parameters.

2.3 NLOS UV Channel Modeling Methodology

2.3.1 Communication Channel Models

In communication systems, a communication channel refers either to a physical transmission medium such as an optical fiber, or to a logical connection over a multipath medium such as a radio channel. Traditionally, information is conveyed from a transmitter to a receiver through a channel. With the progresses of communication theory and signal processing, information transferring between multiple transmitters and receivers is realized in modern communication systems. In the point of communication systems, a channel plays a significant role in information exchanging between a transmitter and a receiver. A lot of channel modeling work has been done. Generally, researchers focus on two important aspects: channel impulse response and channel path loss.

A communication channel acts as a temporal and spatial varying filter which can distort the signal. A channel impulse response shows the reaction of a communication channel in response to an impulse input signal. A channel path loss reveals the

reduction in power level of a transmitted signal as it propagates through the channel. A channel impulse response can be used to further investigate the effects of signal propagation through a communication channel, including multipath propagation delay due to reflections, doppler effects and time of travel for the delay paths. Moreover, path loss can be easily calculated based on a channel impulse response. Path loss, itself, is a major component in the analysis and design of the link budget of a communication system.

For the NLOS UV communication system, we would like to comprehensively investigate the NLOS UV scattering channel by considering both the channel impulse response and path loss. As a result, we will obtain not only time domain information of the NLOS UV channel, but also the received power ratio. All of these results will be valuable for further signal processing and communication algorithm development.

2.3.2 NLOS UV Modeling Methodology

A useful communication channel model will offer great accuracy for system performance prediction and will provide guidelines for system design. Thus channel modeling becomes a critical part in communication system study. Three typical methods are followed to investigate the communication channels. The first one is experimental channel sounding technique which includes time domain sounding and frequency domain sounding. Time domain sounding, also known as a short-pulse technique, uses a short transmitted pulse to directly probe the channel and record the response. Frequency domain sounding, also termed as a continuous wave (CW) swept-frequency technique, uses a constant-amplitude swept-frequency sinusoid to probe the channel. These two channel sounding techniques have been frequently applied for indoor infrared channel measurements [33],[34]. The second method is analytical derivation based on wave prop-

agation theories. For a UV NLOS channel, the radiative transport theory has been used for the analytical single scattering channel model. Transport theory has been widely applied for multiple scattering based on diffusion approximation. However, it only considers power transport in medium [30],[35], and its mathematical complexity in solving a differential and integral equation adds difficulty to channel modeling in the NLOS scenarios. Exact analytical wave propagation theory for multiple scattering put more complexity than transport theory because it starts from Maxwell equation and considers the whole electromagnetic field transmission [30]. Fortunately, there is a close relationship between these two kinds of theories. Our major concern for NLOS UV channel modeling urges us to obtain an analytical solution to fully understand the channel for communication. The third method is a commonly used one which simulates the channel with appropriate mathematical and physical assumptions. For example, Monte Carlo simulations have been frequently employed to investigate indoor infrared communication channel. Good simulation results have been reported worldwide compared with experimental results. For NLOS UV channel, results have been reported by some pioneering researchers. In order to have a full understanding of NLOS UV channel, we focus on characterizing the NLOS UV channel from simulation, analytical formulation, parametric model fitting, and comparing these results with the experimental channel sounding date. Different modeling methods will be adopted in the dissertation to completely investigate the NLOS UV channel. Validation and limitation will also been discussed for different models.

Chapter 3

NLOS UV Channel Measurement and Empirical Modeling

3.1 UV Measurement System

To validate the channel models to be developed, we have experimentally measured both impulse response and path loss, employing a UV pulsed-laser for impulse response and UV LEDs for path loss, respectively. In this section we briefly describe the measurement systems. In the next section we will compare channel models and experimental data.

3.1.1 UV LED Path Loss Measurement System

Chen et. al. [28] and [36] describe a solar blind UV path loss experimental testbed at 260 nm wavelength. As shown in Figure 3.1, the transmitter employed a signal generator to feed a current driver circuit that powered an array of 7 ball-lens UV LEDs. The driving current for each LED was 30 mA, yielding an average radiated optical power of 0.3 mW. Using a beam profiler, the beam divergence angle was measured to be 17^o.

At the receiver, a solar blind filter was mounted on top of the circular sensing window of a Perkin-Elmer PMT module MP1922. The PMT's output current was fed to a high bandwidth preamplifier, whose output was further sent to a photon counter for photon detection. The LEDs, PMT and filter were attached to Tx and Rx angular control modules, respectively. Each module utilized two perpendicular rotation stages to achieve a precise angular control up to 360^o in the azimuth and zenith directions. Experiments reported below have focused on scenarios where the Tx beam axis and Rx FOV axis were coplanar, and only Tx and Rx apex angles were adjusted. The Rx filter had full-width half maximum (FWHM) bandwidth of 15 nm. The filter in-band transmission was 8% and visible-band transmission was below 10^{-10}. The PMT sensing window had a diameter of 1.5 cm, resulting in an active detection area of $\pi(1.5/2)^2 = 1.77cm^2$. The PMT had an average of 10 dark counts per second (10 Hz), and an in-band UV detection efficiency of 13%. Combining the solar blind filter and PMT, the detector's effective FOV was estimated to be 30^o based on the shape and dimension of the filter and PMT.

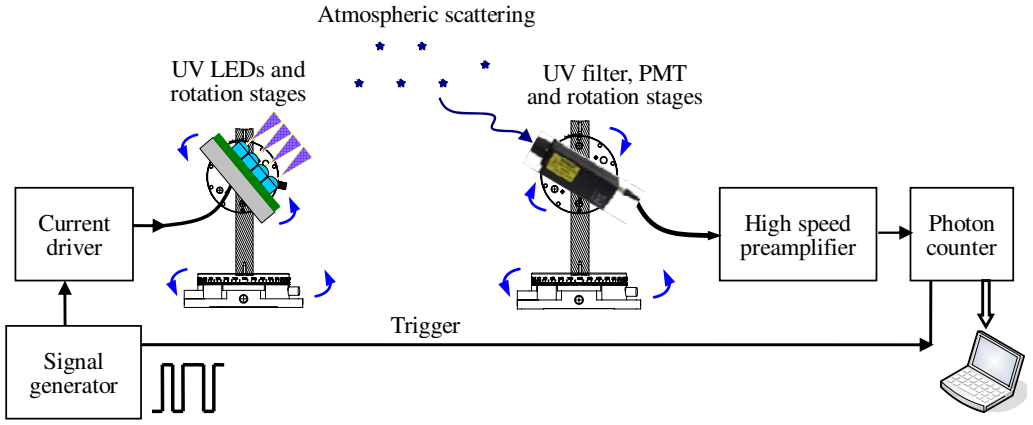

Figure 3.1: NLOS path loss measurement system diagram.

To obtain path loss L, the ratio of transmitted and received power, or $10\log_{10}(P_t/P_r)$

in decibels, was experimentally obtained as follows. In most of the testing configurations, the received power was typically too weak to be measured via a power measurement unit. Consequently, the high sensitivity PMT can be employed for photon counting, and the number of received photons per pulse can be used for calculating L. On the other hand, at the Tx, direct measurement of the total number of emitted photons from the LEDs by a photon counter is impossible because the reading easily overflows the counting limit. Thus, the transmitted optical power was measured using a high performance power meter and the corresponding photon count was calculated from the measured power and wavelength. Each photon carries energy hc/λ where c is the speed of light, h is Planck's constant, and λ is the wavelength. Denoting the transmitted pulse duration as T_p, then the average number of transmitted photons per pulse is $N_t = P_t T_p \lambda/(hc)$. The number of photons detected per pulse is N_d, which is a percentage of the number of photons N_r impinging on the receiver (the solar blind filter in series with the PMT). This is given by $N_d = \eta_f \eta_r N_r$ where η_f is the filter transmission and η_r is the PMT detection efficiency. Finally, the path loss is given by $10 \log_{10}(N_t/N_r)$ dB.

3.1.2 UV Laser Impulse Response Measurement System

Figure 3.2 depicts a solar blind UV communication impulse response test-bed reported by [29]. The critical elements include a high power short-time pulsed UV laser, a high sensitivity PMT detector, and a solar-blind filter with good out-of-band rejection.

The transmitter was a compact Q-switched fourth harmonic Nd:YAG laser at 266 nm triggered by a rectangular pulse at 10 Hz from a signal generator, producing a corresponding laser pulse train at 10 Hz. Each pulse had width of $3 \sim 5$ ns and energy up to $3 \sim 5$ mJ, and can be attenuated manually by a factor of 10^3 with an integrated

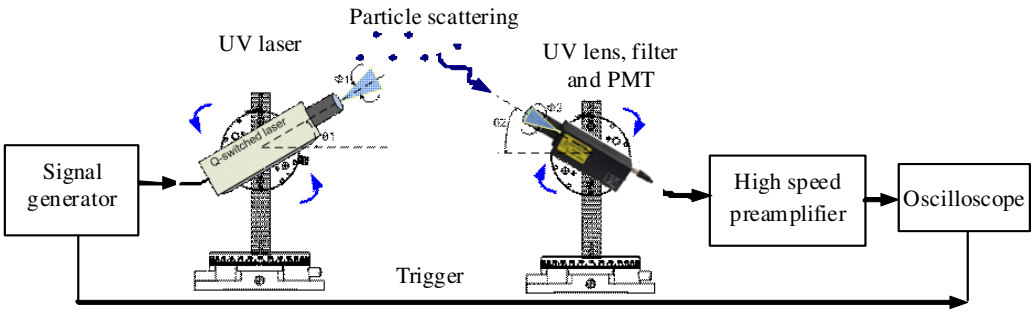

Figure 3.2: NLOS impulse response measurement system diagram.

attenuator. The laser head was mounted on a rotation stage with precise motorized angular control. A synchronization signal from the signal generator was output to the oscilloscope at the receiver through a cable. On top of the laser output window, an optical beam expander and a UV focus lens were mounted to adjust the beam angle. The experimental set of beam angles were obtained via off-line measurements from a set of lenses of different focal lengths.

A pulsed laser UV source was used to provide sufficient power and bandwidth to make direct impulse response measurements. In a typical measurement scenario, at 100 meters baseline range for example, the path loss can exceed 100 dB. No commercial UV laser diodes were available in the solar blind region. Available commercial UV LEDs delivered about 1 mW optical power, with LED arrays extending that up to 50 mW. So these devices did not provide sufficient power for direct impulse response measurement. In addition, the UV LED modulation bandwidths were limited to about 50 MHz, yielding a time domain resolution worse than 20 ns. Consequently, a Q-switched solid state UV laser was employed. A drawback is that the laser could not be modulated at continuously varying frequencies. Therefore, the frequency domain channel sounding technique successfully applied for indoor infrared channel testing is not applicable, and time domain waveform recording techniques had to be used.

At the receiver, the detector was followed by a customized high gain (34 dB) preamplifier module at 1.5 GHz, feeding either an APD or PMT detector. A 3 GHz oscilloscope was used to view and record the detector output waveform. Figure 3.3 shows the receiver response in a LOS configuration with negligible communication distance, for both APD and PMT detectors. The figure shows the APD has a fast response time of about 1 ns, with an FWHM pulse width less than 5 ns. The ripple in the tail was mainly due to electric discharge in the detector circuit. While the APD has a fast response time, its relatively small active area limits gain to about $10^2 \sim 10^4$. Consequently, the APD is not suitable for many high path loss NLOS measurement scenarios of interest due to inadequate weak signal response.

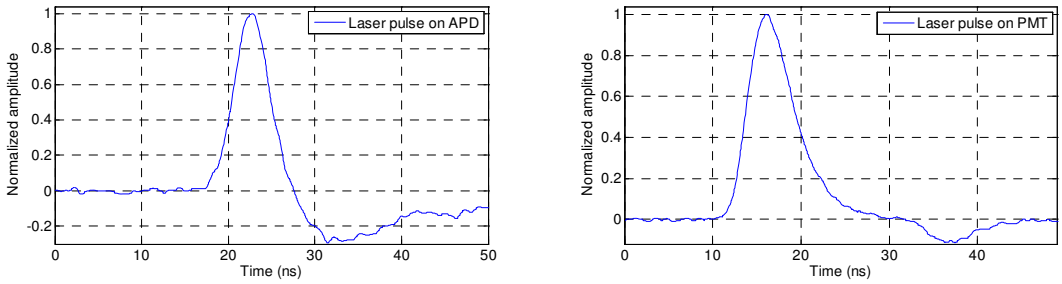

Figure 3.3: APD and PMT photodetector outputs due to an input laser pulse.

Figure 3.3 shows the PMT detector output measured with LOS at negligible range. While the PMT gain is very high ($10^5 \sim 10^7$), its multiple electrode structure tends to spread the response time. The fastest commercial UV PMT available at the time of the experiment was a Hamamatsu PMT whose response time was about 6 ns with an active diameter of 8 mm. The FWHM pulse width was 6.2 ns, and this represented the minimum time resolution in the channel response measurements due to non-ideal devices in the system, including the laser, detector and amplifier circuitry. However, as we will show, the channel response typically spans tens to thousands of nano-seconds.

Consequently, in the impulse response experimental results reported in the next section, we ignore the small smearing introduced by the PMT detection process.

All subsequent results reported are based on a Hamamatsu PMT module H10304 with an integrated high voltage circuit and active diameter of 8 mm, gain 2.3×10^6, and a response time of 6 ns. A focusing lens and a 1-inch solar blind UV filter were mounted before the PMT. The Rx FOV was easily changed by using a set of lenses of different focal lengths, as in the Tx beam angle control. A mechanical module incorporated a rotation stage to achieve high-resolution zenith angular control.

3.2 Path Loss Measurements and Modeling

Consider typical communication geometry, as referring to Figure 2.2. We have conducted extensive test for path loss by varying Tx apex angle, Tx and Rx baseline separation, and Rx apex angle. Beam divergence and FOV are currently fixed, but their effects can be investigated with additional optics to control beam width and FOV. The test distance under a full range apex angle ($Tx\ 0 \sim 90^o, Rx\ 0 \sim 90^o$) is limited to 25 m due to limited transmission power. We also tested distance of 70 m and 100 m at small apex angles ($0 \sim 45^o$). With a laser to be adopted in the future measurements, the range can be significantly extended to a few kilometers. We only focus on LED based short range link path losses in this thesis.

Motivated by the analytical path loss expression under a single scattering assumption [37] that shows a power of r term and an exponential term, we postulate that NLOS UV channel path loss depends on angles and baseline range in a general form of

$$L_{all} = \xi r^{\alpha} e^{\beta r}. \tag{3.1}$$

where parameters of path loss factor ξ, path loss exponent α and attenuation factor

β are all functions of Tx and Rx angles. The power of r term stems from free space path loss, and the exponential term accounts for atmospheric attenuation. Parameter α takes a value of 2 for a point source in a free space LOS link, but reduces to 1 for geometries with large pointing angles. For short range communications upon which our measurements rely, the effect of β is negligible due to the value of attenuation factor in the order of $(1 \sim 10)km^{-1}$ [8]. Its effect may become appreciable when the distance is longer than 1 km. Thus our channel measurement results on path loss for short distance are used to fit the following model

$$L = \xi r^{\alpha}. \tag{3.2}$$

where path loss exponent α and path loss factor ξ are functions of apex angles as follows.

3.2.1 Path Loss Exponent

We tested three distances of 8 m, 15 m and 25 m for a large range of Tx and Rx apex angles. At each distance, we varied both the Tx apex angle θ_1 and the Rx apex angle θ_2 from 0^o to 90^o at a step size 10^o. We recorded the received number of photons and obtained the path loss L for each distance and geometry as the method described before. With those measurements, we applied a curve-fitting technique to estimate path loss exponent α and path loss factor ξ. For example, to find α for any fixed pair of Tx and Rx apex angles, we utilized all path loss measurements at different distances and obtained the ratios $L_i/L_j = (r_i/r_j)^{\alpha}$, for $i, j = 1, 2, 3, i \neq j$. Notice that α is not a function of distance. Then α was estimated from the average of $log_{10}(L_i/L_j)/log_{10}(r_i/r_j)$. For small apex angles, we improved the estimation accuracy by obtaining additional data points corresponding to long distances 75 m and 100 m.

Figure 3.4 shows the path loss exponent α for different Tx and Rx apex angles. It varies from 0.45 to 2.4. For Rx apex angle smaller than 20^o, α is close to 2. In this

case, path loss is very sensitive to distance. For Rx apex angle larger than 70^o, α is either close to 1 or less than 1, leading to low sensitivity to distance. For both Tx and Rx angles close to 90^o, α is around 1, that agrees with results reported in [38].

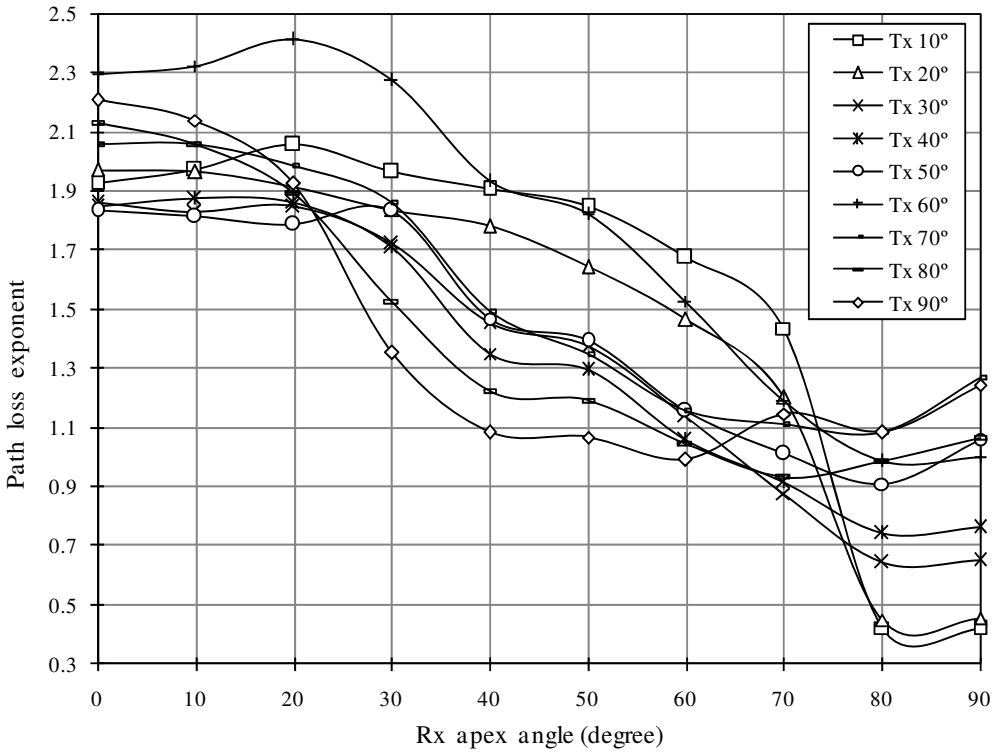

Figure 3.4: Path loss exponent versus Rx apex angle for different Tx apex angles.

3.2.2 Path Loss Factor

The small path loss exponent α corresponding to large Tx and Rx pointing angles does not mean that the total path loss is smaller for a larger pointing angle since it depends on the path loss factor ξ as well. In fact, ξ becomes dominant in the overall path loss as angles increase, as seen from Figure 3.5. It was obtained as an average of all L_i/r_i^α according to Eq. 3.2 and estimated path loss exponent α above. The path loss factor changes by several orders of magnitude for varying Rx pointing angles at any given

Tx pointing angle. The dynamic range under a small Tx pointing angle is larger than that under a large Tx pointing angle. For example, it shows two orders of magnitude change under 90^o Tx pointing angle, but increases to five orders of magnitude under 10^o Tx pointing angle. On the other hand, for a fixed Rx pointing angle, the difference is about three orders of magnitude when Rx pointing angle is small, and less than one order of magnitude when Rx pointing angle is large.

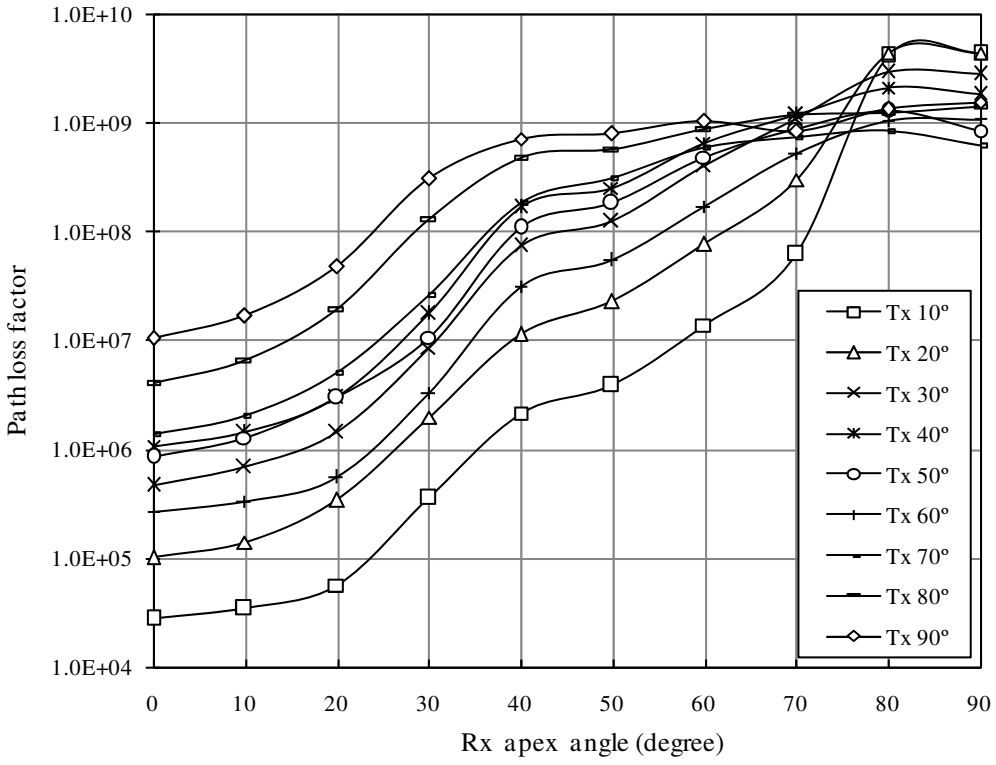

Figure 3.5: Path loss factor versus Rx apex angle for different Tx apex angles.

3.2.3 Path Loss Model Validation

For given Tx and Rx pointing angles and distance within tens of meters, path loss exponent is obtained from Figure 3.4 and path loss factor from Figure 3.5. Then path loss is calculated by Eq. (3.2). The path loss model and results for short range

links can be used to predict path loss for medium communication range, saying up to a few hundred meters.

For model validation, those results can be compared with measurements and an existing single scattering model [4]. Due to a source power constraint, the above model over a large range of pointing angles was obtained from measured data only for short range up to 25 m. When distance increases, only very few settings for small pointing angles led to detectable signals at the detector, and subsequently path loss was obtained. If we tend to generalize the model to cover medium distance, then we can validate it using those finite measured data points.

Figure 3.6 compares predicted with tested path loss for Tx and Rx pointing angles up to 40^o when baseline separation is 100 m. The prediction errors for each Tx pointing angle are within a few decibels over the specified range of the Rx pointing angle.

A single scattering channel impulse response model for NLOS UV communication [4] has been widely adopted to predict path loss for varying distance [37],[38]. Thus the proposed path loss model is also compared with that single scattering based path loss model under different Tx and Rx apex angles in Figure 3.1. For large Tx and Rx pointing angles, the difference between two models is very small. Also from the line slopes, path loss exponent α is found to be 1. This was also verified by experimental results in [28],[38]. For small pointing angles, the single scattering model still provides an unchanged value for α as two lines corresponding to the single scattering model in the figure are observed parallel. That means, the single scattering model predicts a $1/r$ power decay profile irrespective of apex angles. However, α is expected to approach 2 as both Tx and Rx angles approach 0^o, such as LOS [1]. So the single scattering model

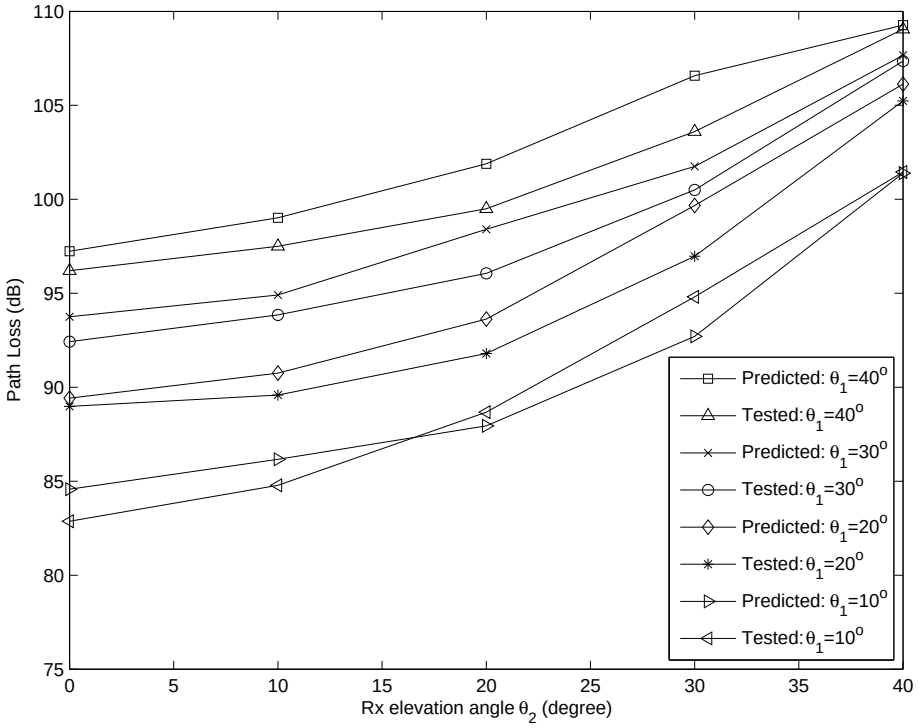

Figure 3.6: Comparison of predicted and tested path loss for different Tx and Rx angles at 100 m distance.

does not predict well the link performance when angles are not large. The proposed model gives $\alpha = 1.88$, close to $\alpha = 2$ and consistent with Figure 3.4. Therefore, it can be concluded that the proposed path loss model predicts link path loss more reliably for a large range of apex angles than the single scattering model. The poor prediction performance of the single scattering model under small apex angles also suggests that a more realistic multiple scattering analytical channel impulse response model is necessary to characterize NLOS link performance under a variety of pointing conditions.

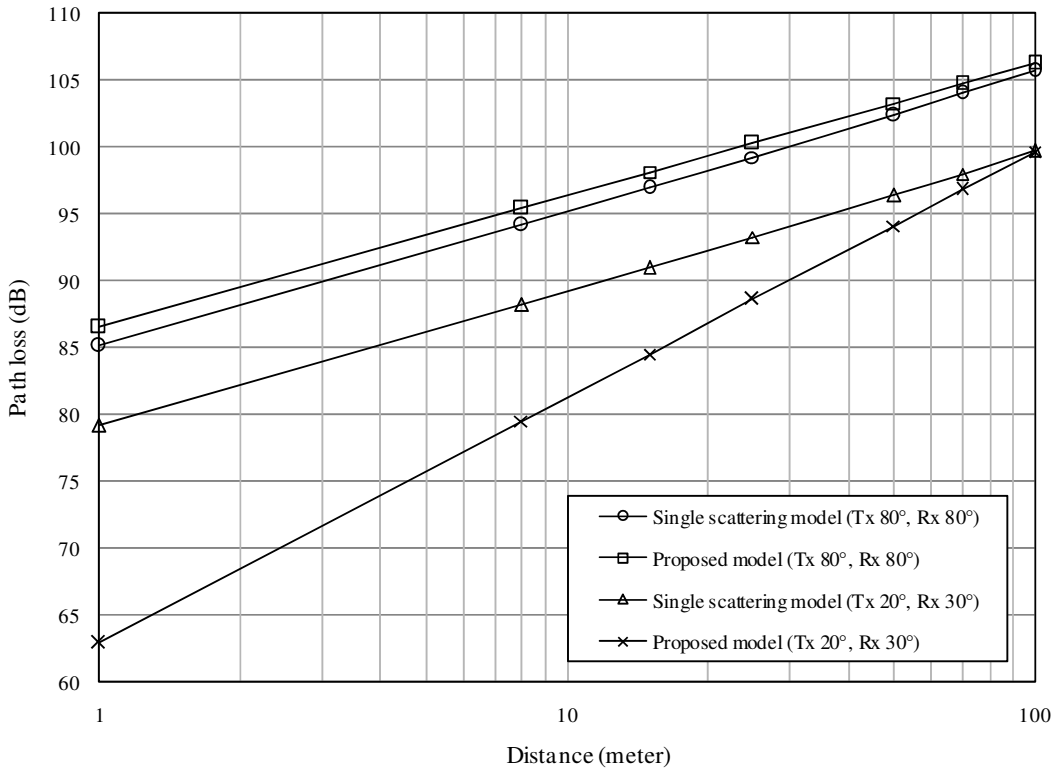

Figure 3.7: Comparison of predicted and tested path loss for different Tx and Rx angles at 100 m distance.

3.3 Impulse Response Measurements

A series of measurements were conducted including varying the Tx and Rx elevation angles from 0^o to 90^o, and changing the Tx beam angle, Rx FOV, and baseline distance up to 100 m. The experimental site was an outdoor open field in clear weather. The laser pulse rate was set at 10 Hz, and the output energy after the optical beam shaping system was 3 mJ. Beam divergence was less than 3 mrad, and line width was 1 cm^{-1}. The 270 nm solar blind filter had FWHM bandwidth of 15 nm. The peak transmission was 10.4% at 271 nm, and the out-of-band transmission was less than 10^{-8} at 290 nm, 10^{-10} at 390 nm, and 10^{-11} at $305 \sim 750$ nm. The spectral mismatch between the laser and the filter was found to be less than 30%. The PMT had a circular sensing window with a diameter of 8 mm, and its dark current was 4 nA. The transmitter's beam

angle was controlled at 3 mrad, 12^o, and 25^o. The receiver's effective FOV without a focus lens was 30^o. It became 13^o, 9.2^o, 4.58^o, and 2^o when using different focus lenses in front of the PMT.

Each measured impulse response exhibits random variation including the changing atmosphere as well as the detector response. We average over realizations to yield the average response for a fixed set of system parameters.

Figure 3.8 shows the normalized waveforms after averaging 1, 5, 10, and 20 realizations in the same geometry, respectively. Note the significant spikes before averaging due to the discrete photon arrivals. The Tx and Rx elevation angles were 40^o and 90^o, beam angle was 3 mrad, the receiver's effective FOV was 30^o, with a baseline distance of 100 m. These results are typical, indicating the measurement variation around the mean behavior. In the following all results are based on averaging over 50 realizations.

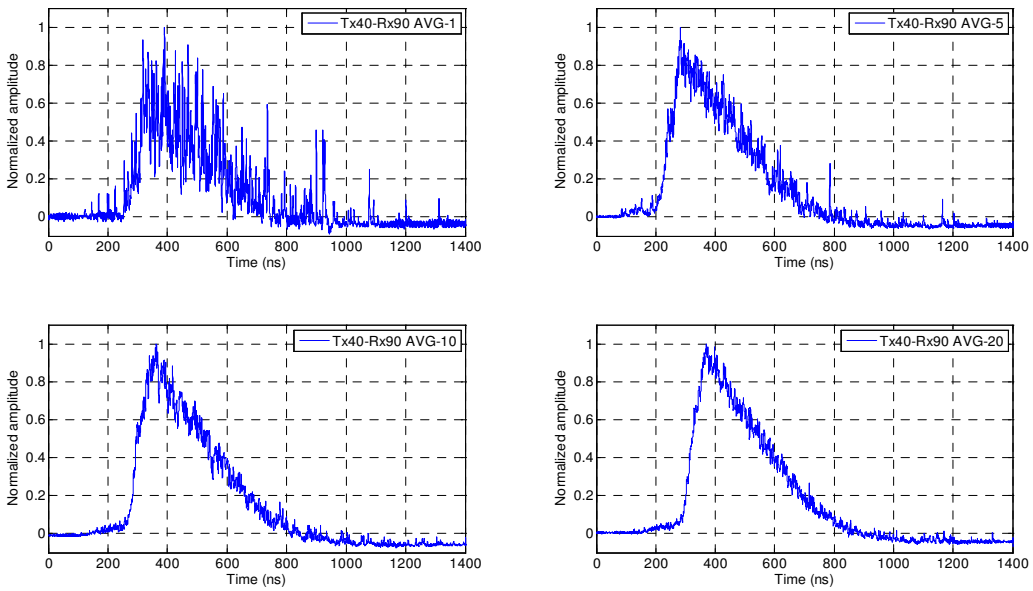

Figure 3.8: Averaged waveform versus time for different number of realizations used for averaging.

While the laser output pulse follows a Gaussian shape, the received waveform varies with different NLOS geometries. To gain some insight, Figure 3.9 shows typical average impulse responses under different Tx and Rx elevation angles, progressing from small angle 10^o to large angle 90^o. The resulting FWHM pulse width varies from 20 ns to 1500 ns. Note the faster rising edge, followed by slower decay. The decay increases as the elevation angle increases, due to the larger spread in propagation times for scattered photons. With a smaller elevation angle (lower to the horizon), the decay becomes significantly sharper and the pulse width is decreased. Note also that, at higher apex angles (approaching vertical pointing), the responses have more variations from measurement to measurement, and the averaged response continues to exhibit significant spread, even after averaging 50 measurements.

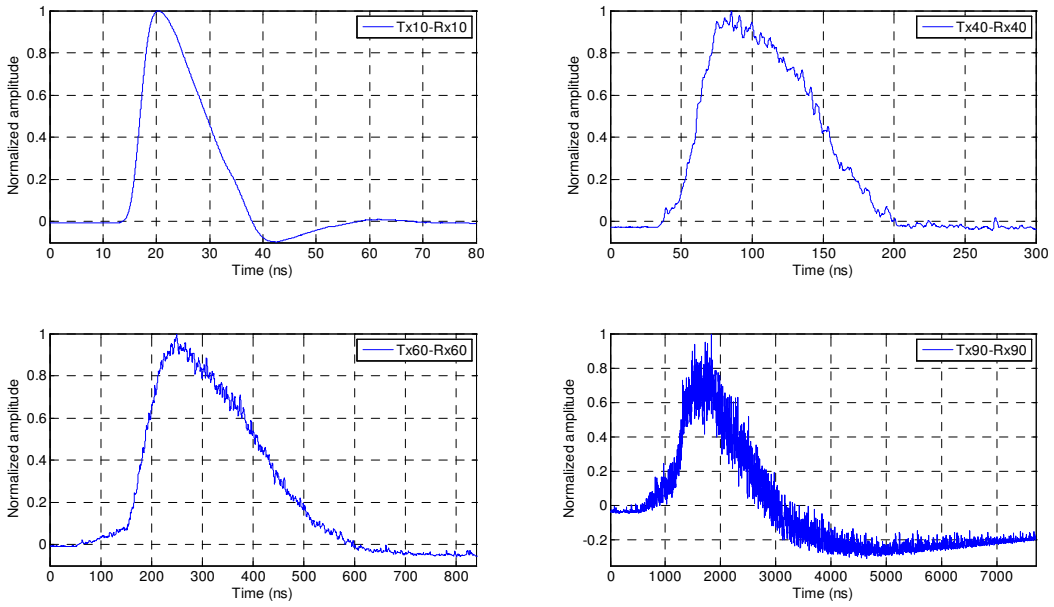

Figure 3.9: Pulse shape with different Tx Rx elevation angle.

Chapter 4

Analytical Modeling and Simulation of UV NLOS Channels

4.1 Single Scattering Model

In this section, we investigate the UV scattering channel for NLOS free space communication links based on a single scattering assumption.

4.1.1 Analytical Single Scattering Model

Single scattering models assume that photons traversing the medium between the Tx and the Rx and impinging on the photodetector undergo scattering at most once. Therefore with this model in NLOS geometry all photons arriving at the detector will have undergone scattering once such that their resulting trajectory lands them in the Rx detector. Paper [17] proposed an analytical single scattering model for a short range NLOS UV scattering channel, and [4] generalized the model to examine angular spectra and path losses. The model assumes an impulse is transmitted, and predicts the atmospheric scattering and extinction, yielding the channel impulse response. The

path loss is then obtained by integrating over the impulse response.

For a NLOS system, the transmitter and receiver are arranged as shown in Figure 2.2. The model is based on a prolate spheroidal coordinate system, illustrated in Figure 4.1. Each point in space is defined by a radial coordinate ξ, an angular coordinate η, and an azimuthal coordinate ϕ. An advantage of this coordinate system is that the sum of the distances between the two foci and any point on a given surface ξ is a constant. This property indicates that a prolate spheroidal surface can be considered as an equitemporal surface, which means that the total single scattering radiation arriving at the receiver at a given time simply requires integration over the surface defined by a given ξ.

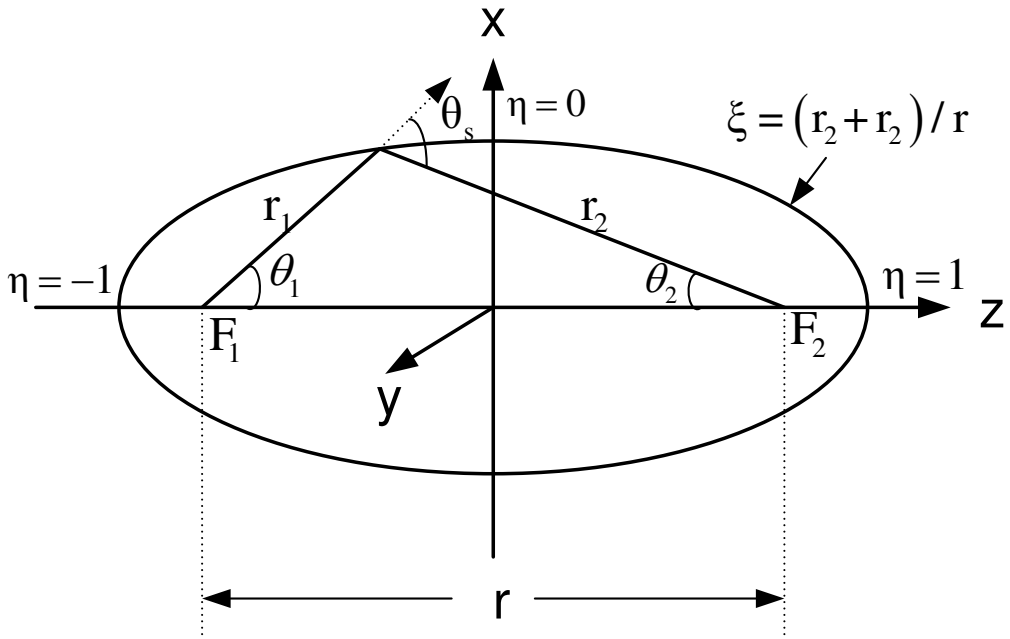

Figure 4.1: Prolate spheroidal coordinate system.

It is assumed that an impulse of energy E_t is emitted at time $t = 0$ uniformly over the transmitter solid cone angle into a homogeneous scattering and ab-

sorbing medium. The system geometry determines the common volume regarding the transmitter and receiver, from which single-scattered photons could reach the receiver. For simplicity, it is assumed that the axes of the transmitter and receiver lie in a common plane (coplanar geometry), and thus the integration volume is symmetric over coordinate ϕ. The received single scattered intensity at time t can be expressed as in [17] and [4]

$$h(t) = \frac{E_t A_r c k_s e^{-k_e ct}}{2\pi\Omega_t r^2} \times \int_{\eta_1(ct/r)}^{\eta_2(ct/r)} \frac{2G[\phi(ct/r,\eta)]p(\theta_s)}{(ct/r)^2 - \eta^2} d\eta, \tag{4.1}$$

where the function $G[\cdot]$ is defined in the cited works.

With reference to Figure 2.2, the parameters and functions are defined as follows. Let Ω_t be the solid angle of the Tx cone, r the Tx - Rx baseline separation, and r_1 and r_2 the distances of the common volume to the Tx and Rx, respectively. Define ϕ_1 and ϕ_2 as the Tx beam angle and Rx FOV, and θ_1 and θ_2 as the Tx and Rx focal angles (interchangeable with elevation angles in this context) between each axis and the horizontal axis. The elevation angles are also referred to as pointing or apex angles. k_e, k_s, k_a are the atmosphere coefficients, θ_s is the scattering angle, A_r is the area of the receiving aperture, and $p(\theta_s)$ the scattering phase function.

4.1.2 A Parametric Single Scattering Channel Model

This above analytical channel model involves complex integration which sometimes would add complicated calculation and hide intuitive information of the channel behavior. As an alternative, we pursue a simple parametric model that allows high fidelity goodness-of-fit test [39]. The development is motivated by a success in modeling the probability density function (pdf) of optical intensity under turbulence [40]. The model adopts a joint gamma function and Laguerre polynomial. Associated parameters are found by minimizing the matching error between the proposed parametric model

and analytical model. For parametric modeling, the gamma function and its modified version are selected as the matching function for the impulse response. Here the two fitting models are expressed in Eq. (4.2) and Eq. (4.3) respectively [39]

$$h_g(t) = A\frac{\beta^{-\alpha}}{\Gamma(\alpha)}t^{\alpha-1}e^{-t/\beta}, \tag{4.2}$$

$$h_{gl}(t) = A\frac{\beta^{-\alpha}}{\Gamma(\alpha)}t^{\alpha-1}e^{-t/\beta}\sum_{i=0}^{N} c_n L_n(t), L_n(t) = \frac{e^t}{n!}\frac{d^n}{dt^n}(e^{-t}t^n). \tag{4.3}$$

In the above, $\Gamma(\alpha)$ is the gamma function, $L_n(t)$ is the n-order Laguerre polynomial, A and c_n are scalar components. In simulation we apply these two parametric models to fit the theoretical model in terms of minimizing the squared matching error. After fitting, we can obtain the unknown parameters in our fitting models and then evaluate modeling performance.

As an example, let's consider a specific geometry: r=100 m, $\phi_1 = \phi_2 = 15^o$, $\theta_1 = \theta_2 = 45^o$, $k_s = 0.49/km$, $k_a = 0.74/km$. Also, different phase functions are included to satisfy different modeling assumptions. Applying these inputs and then minimizing the error between Eq. (4.2) and Eq. (4.1), or between Eq. (4.3) and Eq. (4.1), we can obtain the model parameters and finally channel impulse responses for different phase functions in Figure 4.2.

It can be observed that over a large range of temporal delay spread, the goodness-of-fit test is satisfactory, although there are clearly slight mismatches around each peak and tail. Based on simulation results, we also find the mean-square-errors (MSEs) for two parametric models: 0.0003 for gamma fitting, and 0.00025 for modulated gamma fitting. Two models thus yield low MSEs.

From each parametric model, we can easily obtain the channel frequency response and thus the 3 dB bandwidth. In the case of Rayleigh phase function, we calculate

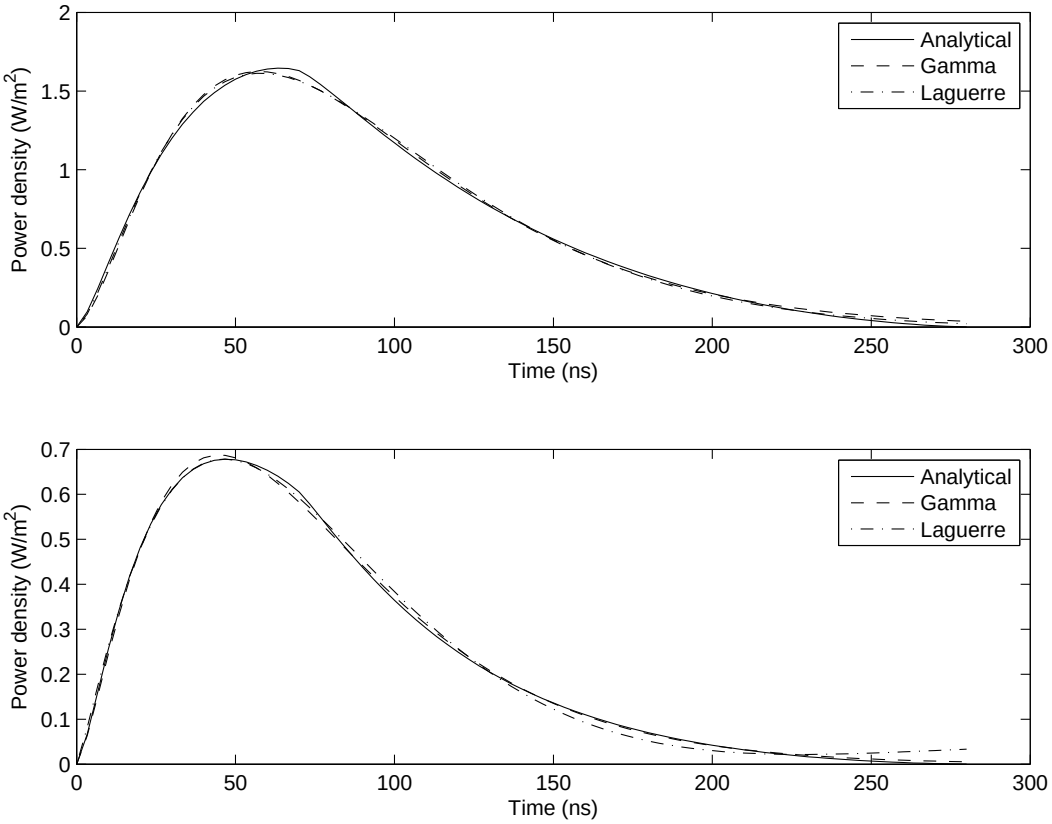

Figure 4.2: NLOS UV impulse responses for Rayleigh and Mie phase functions successively: (a) Rayleigh, (b) Mie.

the 3 dB bandwidth based on the gamma fitting model. From fitting process, we find parameters in Eq. (4.2) as follows: $\beta = 0.0347$, $\alpha = 2.6506$, $A = 0.134$. Its Fourier transform $H_g(f)$ can be derived as

$$|H_g(f)|^2 = \frac{\lambda^2}{(1 + (2\pi\beta f)^2)}. \tag{4.4}$$

Hence, the 3 dB bandwidth for this gamma fitting model is given by

$$B = \frac{\sqrt{(2^{1/\alpha} - 1)}}{2\pi\beta}. \tag{4.5}$$

Using the above numerical values of our fitting model, we can obtain the estimated 3 dB bandwidth as 2.5 MHz. Similarly, applying the same method, we can also derive the bandwidth using the modulated gamma fitting model.

4.1.3 Approximate Single Scattering Path Loss Model

The impulse response model in Eq. (4.1) does not lead to a tractable closed form and so requires numerical analysis. We can obtain a closed form approximation for $h(t)$ that is amenable to incorporation into communications performance analysis, as follows. The derivation assumes that the geometry is such that the intersecting cones are small. Following the geometry and parameters defined above, the energy at the Rx scattered from the differential volume dV in V can be modeled as [37]

$$\delta E_r = \frac{E_t k_s P(\mu) A_r \delta V \cos(\zeta) e^{-k_e(r_1+r_2)}}{\Omega_t r_1^2 r_2^2}, \tag{4.6}$$

where ζ is the angle between the Rx axis and a vector from the Rx to the common volume, and phase function $P(\mu)$ is given by Eq. (2.1). The total energy at the receiver can be found by integrating over the common volume using the prolate spheroidal coordinate system, but this requires numerical evaluation. To obtain a tractable analytical expression, we assume that the common volume is small so that $\zeta \approx 0$, and use this to simplify $h(t)$ and the resulting expression for the total received energy. Note that $\Omega_t = 2\pi(1 - \cos\frac{\phi_1}{2})$, $r_1 = r\sin\theta_2/\sin\theta_s$, $r_2 = r\sin\theta_1/\sin\theta_s$, and $\theta_s = \theta_1 + \theta_2$. Now, we can approximate the total received energy as

$$E_r \approx \frac{E_t k_s P(\mu) A_r V \sin^4\theta_s \exp[-\frac{k_e r}{\sin\theta_s}(\sin\theta_1 + \sin\theta_2)]}{2\pi r^4 \sin^2\theta_1 \sin^2\theta_2 (1 - \cos\frac{\phi_1}{2})}. \tag{4.7}$$

Define the path loss as the energy ratio $L = \frac{E_t}{E_r}$. Here L depends on the common volume V that in turn depends on the shape of the intersection. For a small overlap volume, V can be well approximated by a frustum[1] of the right cone of volume $V = \frac{1}{3}\pi(D_1^2 h_1 - D_2^2 h_2)$, where $h_1 = r_1 + r_2\frac{\phi_2}{2}$ and $D_1 = h_1\frac{\phi_1}{2}$ are the height and the radius of the bottom surface of the large cone, and $h_1 = r_1 - r_2\frac{\phi_2}{2}$ and $D_2 = h_2\frac{\phi_1}{2}$ for

[1]The frustum is the portion lying between two parallel planes.

the smaller cone. Both cones share a common apex at the Tx location. Substituting r_1, r_2 and θ_s into V and the corresponding result into Eq. (4.7), we obtain the following path loss expression

$$L \approx \frac{96r \sin\theta_1 \sin^2\theta_2 (1 - \cos\frac{\phi_1}{2}) \exp[\frac{k_e r(\sin\theta_1 + \sin\theta_2)}{\sin\theta_s}]}{k_s P(\mu) A_r \phi_1^2 \phi_2 \sin\theta_s (12\sin^2\theta_2 + \phi_2^2 \sin^2\theta_1)}. \tag{4.8}$$

This provides L as an explicit function of the system and geometric parameters, and is easily applied to link analysis for a particular choice of the atmospheric parameters. However, this model only provides high fidelity path loss approximations when the common volume is small, which limits its applicability for geometries with longer baseline range or large common volume overlap such as can occur with wide optical field of view.

4.2 Multiple Scattering Models

Next we remove the single scattering assumption, and describe models that allow multiple scattering. Generally, higher atmospheric particle density and longer propagation range lead to a higher probability of multiple scattering, and atmospheric particles can be quite abundant and reactive to UV photons. Thus, in some cases, a multiple scattering model can lead to more accurate channel prediction, and the model enables separation and study with respect to the scattering order effect.

As we will show, multiple scattering interactions of photons with the atmospheric constituents result in additional pulse broadening beyond that due to single scattering, i.e., there is increased channel delay spread. The additional pulse spreading occurs because, with multiple scattering, longer path lengths are possible. The pulse spreading limits the channel bandwidth available for communications due to the introduction of inter-symbol interference (ISI). Accounting for multiple scattering also

enables more accurate prediction of path loss. With multiple scattering there are more opportunities for photons to successfully transit from the Tx to the Rx, so that the predicted path loss under the multiple scattering model is generally less than that from the corresponding single scattering path loss model. These channel characteristics are a function of transmitter-receiver geometry, including transmitter beam width, elevation angles, range, and receiver FOV. While these are crucial for UV NLOS communications system performance analysis, there is no simple closed-form multi-scattering NLOS UV channel model. In this section, first we review a Monte Carlo numerical technique to obtain both the impulse response and the corresponding path loss, and then we consider an analytical solution for the path loss.

4.2.1 Numerical Monte Carlo Multiple Scattering Channel Model

The method described here computes the impulse response due to multiple scattering via Monte Carlo (MC) simulation of each photon's arrival probability along with the associated propagation delay to the Rx. Path loss can then be easily obtained from the area under the impulse response curve as illustrated by [41], [42].

Following [43], the main idea of the MC method is to simulate a complex process as a succession of elementary events whose probability laws are known. Light is decomposed into a set of photons and each individual photon's migration path is probabilistically modeled. This process is repeated for a large number of photons, yielding a statistical picture of the propagation channel. After emission, each photon will follow a migration path along which it may be scattered and/or absorbed. The length of each migration between scattering events is governed probabilistically, as is the departure angle after scattering. Each photon has an initial survival probability that is renewed after each migration. The photon is repeatedly migrated until it either reaches the receiver

or its survival probability is smaller than a threshold value whereupon it is considered lost. The process is repeated for many photons, and the aggregated arrival probabilities as a function of time represent the expected received signal intensities, corresponding to the channel impulse response. Figure 4.3 shows a block diagram of the Monte Carlo simulation method, whose details are described next.

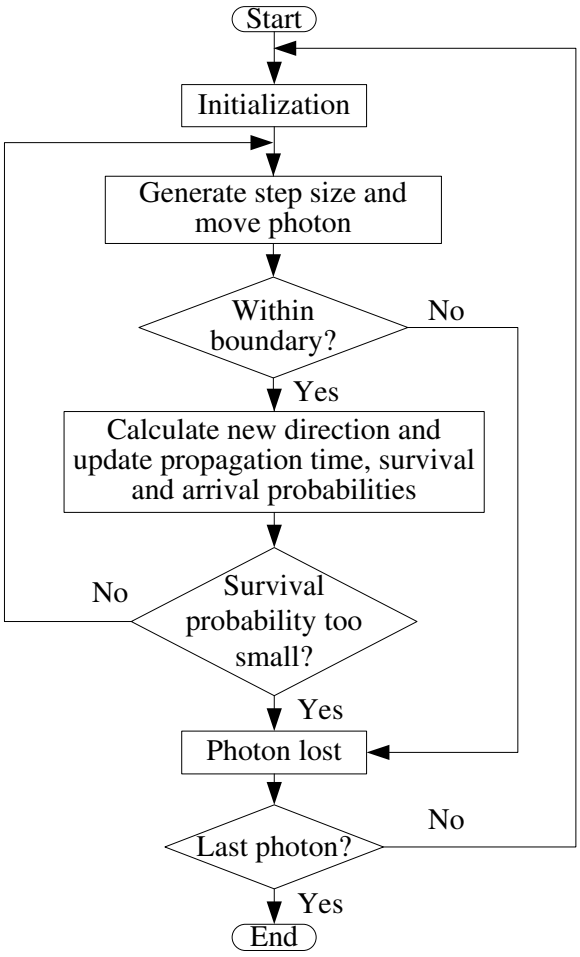

Figure 4.3: Monte Carlo Algorithm for multiple scattering impulse response.

The Monte Carlo method begins by launching a photon from the light source located at $\underline{r}_0$ into the channel. A collimated or divergent source can be modeled. For the configuration shown in Figure 2.2, each photon's initial direction must be confined

within the full beam angle ϕ_1 with solid angle $2\pi(1-\cos\frac{\phi_1}{2})$. We place the light source in the coordinate system such that the beam axis has a zenith angle $(\pi/2-\theta_1)$ and azimuth angle 0^o. Let the initial direction of an individual photon with respect to the zenith angle be θ_{ini}, and with respect to the azimuth angle be ψ_{ini}. Then, the initial direction from the beam axis is

$$U = \theta_{ini} - (\pi/2 - \theta_1).$$

For a uniformly distributed light source, the initial angles are generated to satisfy

$$\begin{aligned} \cos U &= 1 - \xi^{(\theta)}(1-\cos\frac{\phi_1}{2}), \\ \psi_{ini} &= 2\pi\xi^{(\psi)}, \end{aligned} \tag{4.9}$$

where $\xi^{(\theta)}$ and $\xi^{(\psi)}$ are independent standard uniform random variables (uniform between zero and one).

The photon trajectory is then simulated by successive migration paths among different scattering centers. After each interaction between a photon and a scattering center, the photon's propagation is assumed to follow the law of single scattering until it reaches the next scattering center or arrives at the receiver. Following this theory, the distance between scattering interactions is given by the random variable

$$\Delta s = -\frac{\ln\xi^{(s)}}{k_s}, \tag{4.10}$$

where $\xi^{(s)}$ is a standard uniform random variable.

An individual photon's spatial migration path can be uniquely described by five variables: three spatial coordinates for the position and two direction angles θ and ψ. The photon's spatial position can be represented with three Cartesian coordinates and the migration direction can be described with three direction cosines from the two direction angles. The direction cosines are specified by taking the cosines of the

angles that the photon's direction makes with each of the x, y, and z axes, respectively. As an example, the initial direction cosines are specified by $\mu_x^{ini} = \cos\psi_{ini}\sin\theta_{ini}$, $\mu_y^{ini} = \sin\psi_{ini}\sin\theta_{ini}$, and $\mu_z^{ini} = \cos\theta_{ini}$. For a photon located at (x_i, y_i, z_i) travelling a distance Δs in the direction (μ_x^i, μ_y^i,μ_z^i), its coordinates are updated in the 3-dimensional geometry by

$$\begin{aligned} x_{i+1} &= x_i + \mu_x^i \Delta s, \\ y_{i+1} &= y_i + \mu_y^i \Delta s, \\ z_{i+1} &= z_i + \mu_z^i \Delta s. \end{aligned} \tag{4.11}$$

The new migration direction is governed by the normalized phase function that describes the angular intensity of scattered light. When applied to a single photon, this describes the scattered direction (the scattering angle). The deviation from the current direction is determined from a standard uniform random variable $\xi^{(\mu)}$ and the phase function by [44]

$$\xi^{(\mu)} = 2\pi \int_{-1}^{\mu_1} P(\mu) d\mu. \tag{4.12}$$

Here, $\mu_1 = \cos\theta$, where θ is the angle of the new photon path with respect to the current direction. A numerical solution for θ can be obtained from Eq. (4.12). Note that because there is no azimuth dependence in the phase function, the azimuth angle ψ is then set as a uniformly distributed random variable between 0 and 2π, and so this step provides both angles θ and ψ.

The next step is to compute the direction cosines in the absolute Cartesian coordinate system previously described. If a photon is scattered at angles (θ,ψ) offset from the incoming direction with direction cosines (μ_x^i, μ_y^i, μ_z^i), then the new direction

cosines are easily calculated via

$$\mu_x^{i+1} = \frac{\sin\theta}{\sqrt{1-(\mu_z^i)^2}}(\mu_x^i\mu_z^i\cos\psi - \mu_y^i\sin\psi) + \mu_x^i\cos\theta,$$

$$\mu_y^{i+1} = \frac{\sin\theta}{\sqrt{1-(\mu_z^i)^2}}(\mu_y^i\mu_z^i\cos\psi + \mu_x^i\sin\psi) + \mu_y^i\cos\theta,$$

$$\mu_z^{i+1} = -\sin\theta\cos\psi\sqrt{1-(\mu_z^i)^2} + \mu_z^i\cos\theta. \tag{4.13}$$

Each photon is assigned a survival probability, initialized to one when first emitted by the source. The probability that the photon arrives at the receiver within its FOV after n scattering steps is given by

$$p_{1n} = \int_{\Omega_n} P(\cos\theta)\delta\Omega, \tag{4.14}$$

where Ω_n is the solid angle along the scattered direction that can be seen by the receiver aperture of area A_r, and $P(\cdot)$ is the phase function defined earlier. The probability that the photon cannot be seen by the receiver (i.e., it moves out of the receiver FOV) is thus $(1-p_{1n})$.

Between scattering interactions, the photon is modeled to move with a random step size, and along this path we next consider energy loss between two consecutive scatter centers. The photon location changes from the $(n-1)$-th scattering center location r_{n-1} to the n-th scattering center location r_n according to the direction cosine and coordinate updates described above. Between these scattering centers, the propagation distance $|r_n - r_{n-1}|$ is given by the random variable Δs in Eq. (4.10). Along this path between scatterers, the photon undergoes an energy loss of $e^{-k_a|r_n-r_{n-1}|}$, which is a function of k_a. Impinging upon the n-th scattering center, the photon's survival probability is reduced due to this energy loss and so is updated according to

$$w_n = (1-p_{1n})e^{-k_a|r_n-r_{n-1}|}w_{n-1}. \tag{4.15}$$

After the n-th scattering interaction, the probability that the photon successfully arrives at the receiver is given by

$$\mathcal{P}_n = w_n p_{1n} p_{2n}, \tag{4.16}$$

where p_{2n} represents the propagation loss of the photon from the n-th scattering center to the receiver

$$p_{2n} = e^{-k_e |r_n - r'|}, \tag{4.17}$$

r' is the location vector of the receiver, and k_e is employed to model the path loss.

To calculate the channel impulse response, it is necessary to find the propagation time (i.e., relative time delay) of each photon, in addition to its probability of arrival at the detector. This is easily found from the photon migration path, and is given by d_n/c, where d_n is the accumulated propagation distance $d_n = \sum_{j=1}^{n} |r_j - r_{j-1}|$ and c is the speed of light. For example, suppose a photon undergoes N scattering interactions. Then, associated with this photon are a set of probabilities ($\mathcal{P}_1$, $\cdots$, $\mathcal{P}_N$), and a corresponding set of propagation times between each pair of scatterers. The Monte Carlo procedure is carried out for a large number of photons (e.g., $M = 10^6$ or more). To display the expected impulse response, the probabilities are superimposed. If we denote each photon energy by E_p, then the probabilities versus time represent the channel response due to M photons. The curve is normalized by $E_P M$ to obtain the impulse response corresponding to a transmitted pulse with energy equal to one joule.

4.2.2 Analytical Multiple Scattering Path Loss Model

Following the same physical scattering law as the Monte Carlo technique, [45] proposes a stochastic analytical method to theoretically derive the n-th order scattered signal energy collected by the detector. The model considers all photons to be stochasti-

cally scattered and/or absorbed by the atmospheric particles, and involves probabilistic modeling of the photon direction, distance, energy loss, and receiver capture for a specified scattering order. In order to obtain the n-th order scattered signal at the receiver, we trace the migration route of a single photon through the medium. The migration distance and scattering angles follow probability distribution functions (PDFs) that are determined by Beer's law and the phase function, respectively. The PDF of the migration distance r is given by

$$f_r(r) = k_s e^{-k_s r}. \tag{4.18}$$

The zenith scattering angle under combined Rayleigh and Mie scattering has the following PDF

$$f_\theta(\theta) = \frac{k_s^{Ray}}{k_s} f_\theta^{Ray}(\theta) + \frac{k_s^{Mie}}{k_s} f_\theta^{Mie}(\theta), \tag{4.19}$$

where $f_\theta^{Ray}(\theta)$ and $f_\theta^{Mie}(\theta)$ are the phase functions, and θ takes values in $[0, \pi]$. We consider a uniform distribution between 0 and 2π for azimuth scattering angle ϕ because there is no azimuth dependence in the phase function (symmetry is assumed). Thus, the azimuth scattering angle PDF is simply

$$f_\phi(\phi) = \frac{1}{2\pi}, \quad \phi \in [0, 2\pi]. \tag{4.20}$$

Assume a photon from a UV emitter is uniformly emitted at initial direction angles θ_0 and ϕ_0 within the beam divergence, and migrates a distance r_0 before the first scattering occurs. The solid angle within the beam can thus be modeled as a uniform random variable with a constant PDF of $1/\Omega_t$, where Ω_t is the source beam solid angle given by $\Omega_t = 2\pi(1 - \cos\frac{\phi_t}{2})$. In the current context, we use $(\phi_t, \phi_r, \theta_t, \theta_r)$ as Tx beam width, Rx FOV, Tx and Rx pointing angles respectively, not confusing with notations in Figure 2.2. The probability that it is scattered in the infinitesimal solid angle $d\Omega_0 = \sin(\theta_0) d\theta_0 d\phi_0$ becomes $1/\Omega_t \sin(\theta_0) d\theta_0 d\phi_0$, and the probability that it

moves an incremental distance dr_0 with attenuation is $e^{-k_a r_0} f_{r_0}(r_0) dr_0$. Therefore the probability that this photon lies away from the scatter center by r_0 and further moves dr_0 along the infinitesimal solid angle is the product of these two probabilities

$$dQ_0 = \frac{e^{-k_a r_0}}{\Omega_t} f_{r_0}(r_0) \sin(\theta_0) d\theta_0 d\phi_0 dr_0. \tag{4.21}$$

After arriving at the first scattering center, the photon is scattered and then continues to move with attenuation. The scattering center is regarded as a secondary point source emitting photons spatially following the scattering angle PDFs described by Eqs. (4.19) and (4.20). From the i-th scattering center to the $(i+1)$-th scattering center ($i = 1, 2, \cdots$), a similar small probability dQ_i conditioned on all previous events can be written as

$$dQ_i = e^{-k_a r_i} f_{r_i}(r_i) f_{\theta_i}(\theta_i) f_{\phi_i}(\phi_i) \sin(\theta_i) d\theta_i d\phi_i dr_i. \tag{4.22}$$

The same procedure can be successively applied for each scattering process. We assume each scattering is self-governed, and the distances and angles for different scattering events are conditioned on previous quantities. Therefore, the arrival probability for a photon that is scattered n times before arriving at the Rx can be derived based on these transitions. Figure 4.4 shows the photon trajectory corresponding to n possible scatterings.

After the n-th scattering, we focus on an infinitesimal solid angle within the receiver FOV for the receiver to obtain this photon. Let the direction angle ψ_n be the angle between the line connecting the receiver and the n-th scattering center, and the transmitter-receiver separation line. Since the FOV has angular range of $[\theta_r - \phi_r/2, \theta_r + \phi_r/2]$, we can confine the photon direction using an indicator function I_n, which equals one when the condition $(\theta_r - \phi_r/2) < \psi_n < (\theta_r + \phi_r/2)$ is satisfied and zero otherwise.

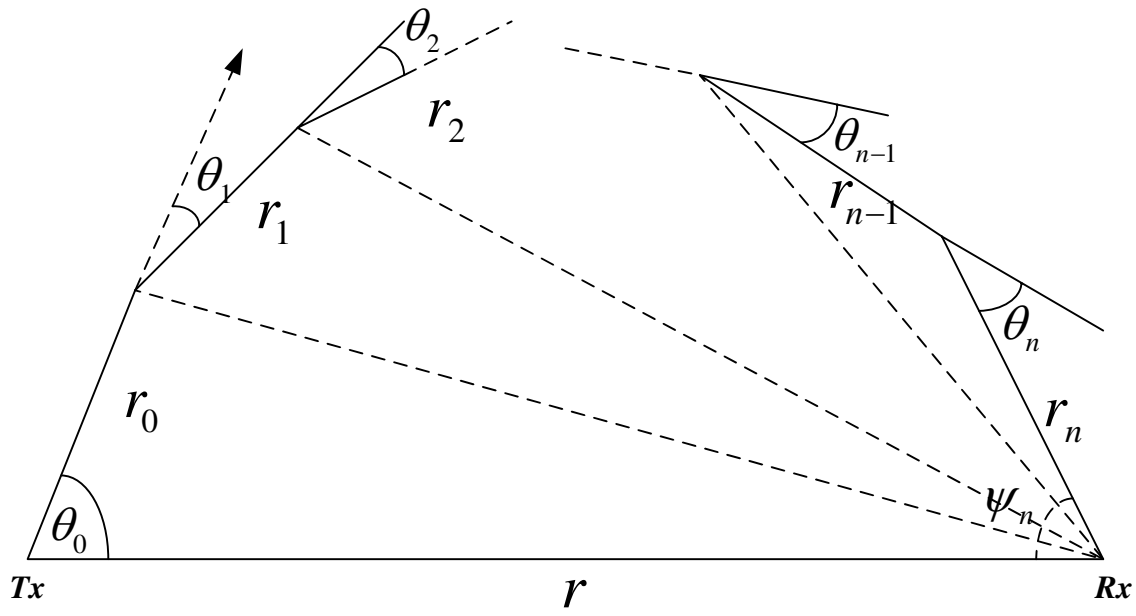

Figure 4.4: Photon migration path for n-th order scattering.

Therefore, the probability of the photon leaving the n-th scattering center and reaching the detector is

$$dQ_n = I_n e^{-k_e r_n} f_{\theta_n}(\theta_n) f_{\phi_n}(\phi_n) \sin(\theta_n) d\theta_n d\phi_n. \tag{4.23}$$

The photon arrival probability after n scatterings is denoted P_n, given by

$$P_n = \int \int \cdots \int dQ_0 \times dQ_1 \cdots \times dQ_n. \tag{4.24}$$

If the UV source emits a pulse with energy E_t, then the received total energy up to n scatterings is

$$E_{r,n} = \sum_{i=1}^{n} E_r(i) = E_t \sum_{i=1}^{n} P_i, \tag{4.25}$$

and the corresponding path loss can be expressed as

$$PL_n = \frac{E_t}{E_{r,n}} = \frac{1}{\sum_{i=1}^{n} P_i}. \tag{4.26}$$

We typically express the path loss in decibels, given by $10 \log_{10}(PL_n)$. As n goes to ∞, the energy represents the total possible over all scattering orders. Later we will

consider some specific cases. Sometimes single scattering dominates, while for some cases scattering up to about 4th-order can make a meaningful contribution.

4.3 Analysis of Modeling Performance

In this section we evaluate the channel models for some cases of interest, and compare them with experimental measurements taken as described in the previous section.

4.3.1 Numerical results

Table 4.1 compares properties for the four models: Reilly's single scattering model, our closed form approximation to Reilly's model (labeled "Approximation" in the table), our Monte Carlo simulation (labeled "Monte Carlo"), and our analytical path loss model (labeled "Analytical"). The Monte Carlo technique is the most generally applicable, incorporating multiple scattering and yielding both path loss and impulse response estimates. The multi-scattering analytical model yields an expression for the distribution of the probability of photon detection, but we do not have a closed form for the expectation over this distribution, hence the need for the Monte Carlo approach.

Paper [45] evaluated the models described above for the impulse response and path loss, varying the geometry including range, and Tx and Rx angles. The parameters

Table 4.1: Scattering model comparison

Model property	Reilly	Approximation	Monte Carlo	Analytical
Closed form	No	Yes	No	No
Multiple scattering	No	No	Yes	Yes
Impulse response	Yes	No	Yes	No
Path loss	Yes	Yes	Yes	Yes
Arbitrary geometry	Yes	No	Yes	Yes

Table 4.2: Atmosphere model parameters: tenuous, thick and extra thick conditions

atmosphere	$k_s^{Ray}(\text{km}^{-1})$	$k_s^{Mie}(\text{km}^{-1})$	$k_a(\text{km}^{-1})$
tenuous	0.266	0.284	0.972
thick	0.292	1.431	1.531
extra thick	1.912	7.648	1.684

were chosen to be realistic with respect to our experimental measurement systems. We assume gas concentrations and optical features of the atmosphere as described by Table II of [31] for middle UV at wavelength 260 nm. As we might expect, variation in the absorption and Mie scattering coefficients indicate that weather conditions may significantly affect the UV signal propagation. However, an explicit correspondence between the parameter settings and weather conditions is not available in the literature. Therefore we consider atmosphere coefficients for three cases: typical tenuous, thick, and extra thick atmosphere conditions (corresponding to clear, overcast, and foggy), given in Table 4.2. The tenuous condition will be adopted for all the following results unless stated otherwise.

Figure 4.5 shows a Monte Carlo simulated impulse response (solid curve). The geometric and model simulation parameters were set as follows: $(\phi_1,\phi_2,\theta_1,\theta_2) = (17^o,30^o,90^o,90^o)$, range r at 100 meters, $\gamma = 0.017$, $g = 0.72$, $f = 0.5$ and the detector area is $1.77cm^2$. Also shown for comparison is a single scattering impulse response model, given by Eq. (3.13a) in [4]. Note that the multiple scattering model predicts both higher intensity and longer duration than the model based on a single scattering assumption, which generally underestimates the effect of scattering.

The multiple scattering path loss for an extra thick (e.g., foggy) atmosphere is plotted in Figure 4.6 for four different pointing angle pairs, with the baseline range

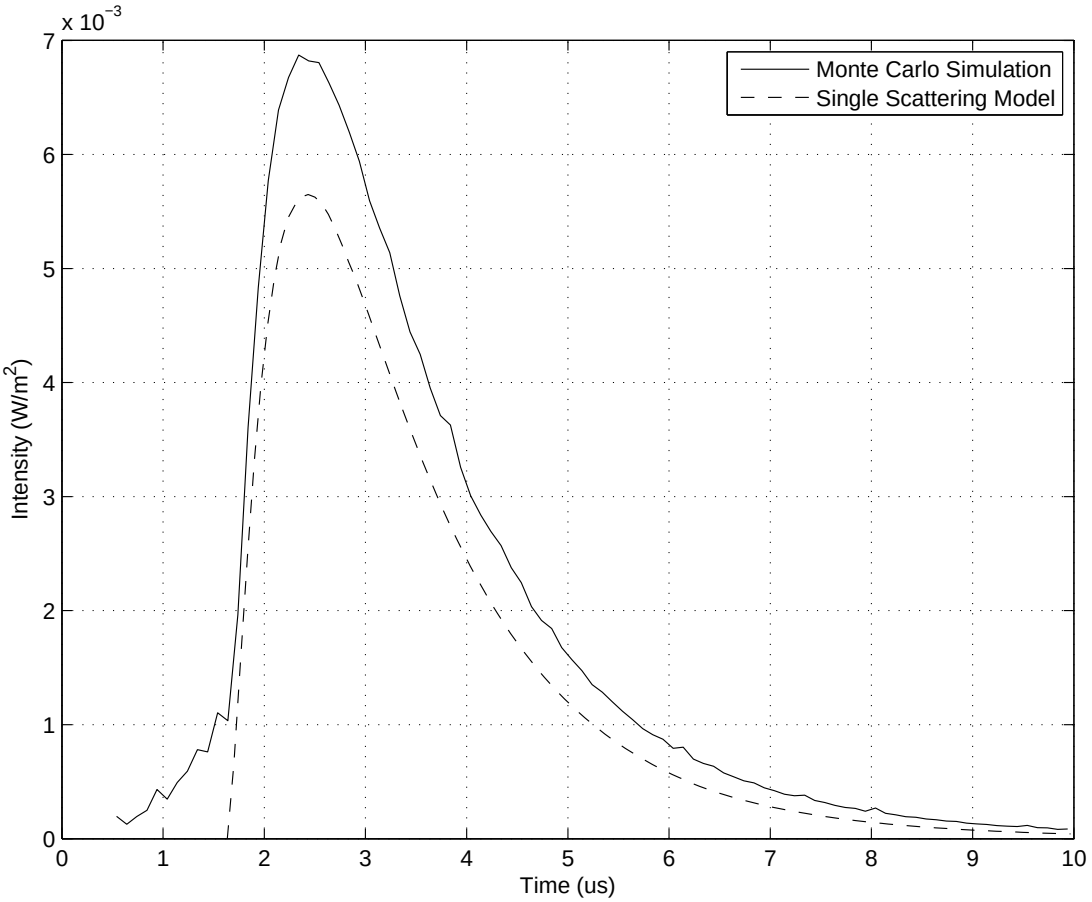

Figure 4.5: Simulated impulse response under single and multiple scattering assumptions. The single scattering assumption yields lower delay spread and intensity.

varying from 10 to 1000 meters. The higher order scattering in this example is enhanced due to the thick atmosphere assumption, and highlights the need to account for higher order scattering in some scenarios. The path loss generally increases as the pointing angles become more vertical, proceeding from panels (a) to (d). The curves are parameterized by scattering order n, and indicate the predicted decrease in path loss as higher order scattering is incorporated. In these examples, the path loss in decibels does not significantly decrease for scattering orders above $n = 4$. Note in Figure 4.6(d) that with vertical pointing angles multiple scattering ($n > 1$) predicts dramatically less path loss than the single scattering ($n = 1$) model.

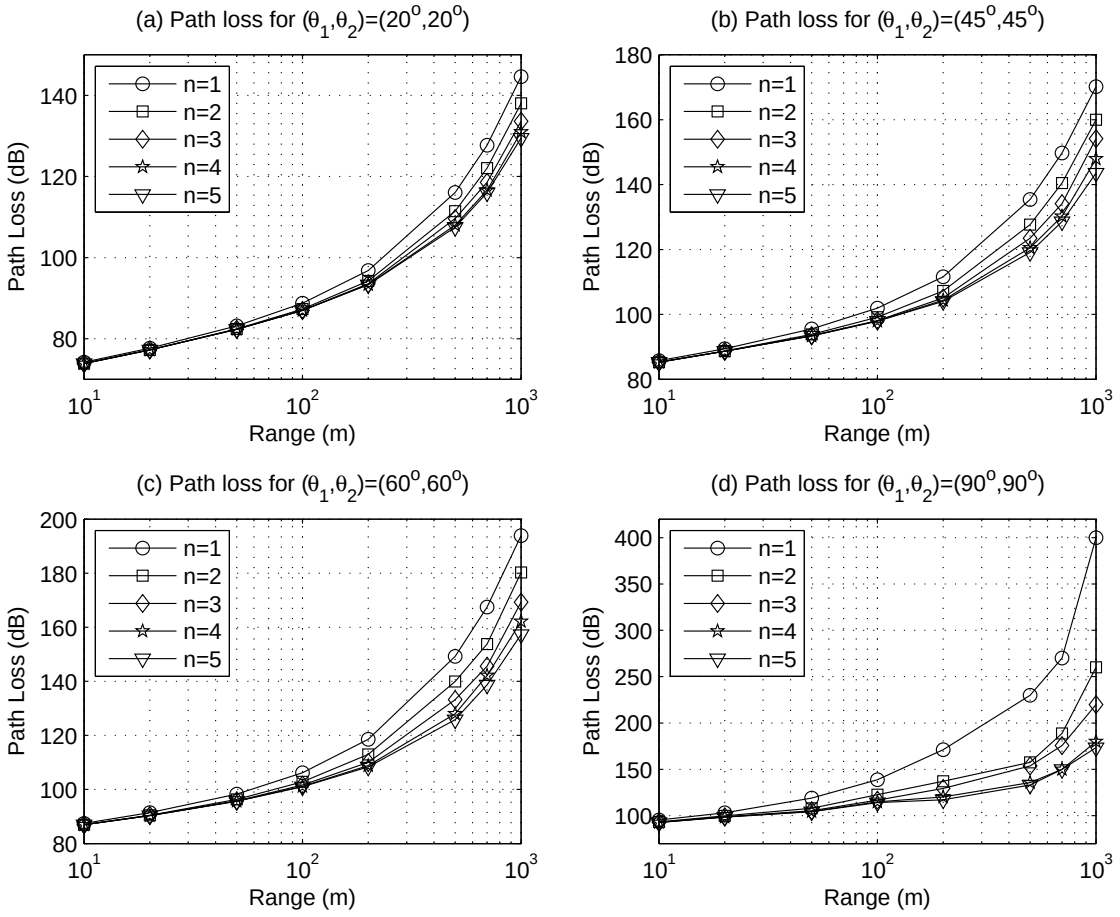

Figure 4.6: Predicted path loss for an extra thick atmosphere.

4.3.2 Experimental Results and Comparison with Simulation

The calibration of our NLOS measurement system was performed in a line-of-sight (LOS) configuration as reported in [36]. Many measurements of path loss and impulse response have been taken outdoors using the systems described in the previous section. We report on some of these, and compare with simulated channel response.

Using a UV LED source array, a variety of path loss measurements were carried out with different Tx/Rx geometries and separation distances. The path loss was calculated as the ratio between the transmitted photons radiated from the UV LEDs and the signal photons impinging upon the receiver. The former was calculated based

on the measured source radiated power, and the latter was calculated from measured received photons divided by the total percentage loss from the filter and PMT with receiving area of $1.77cm^2$. If the path loss per unit area is of interest, then the results can be normalized by this area.

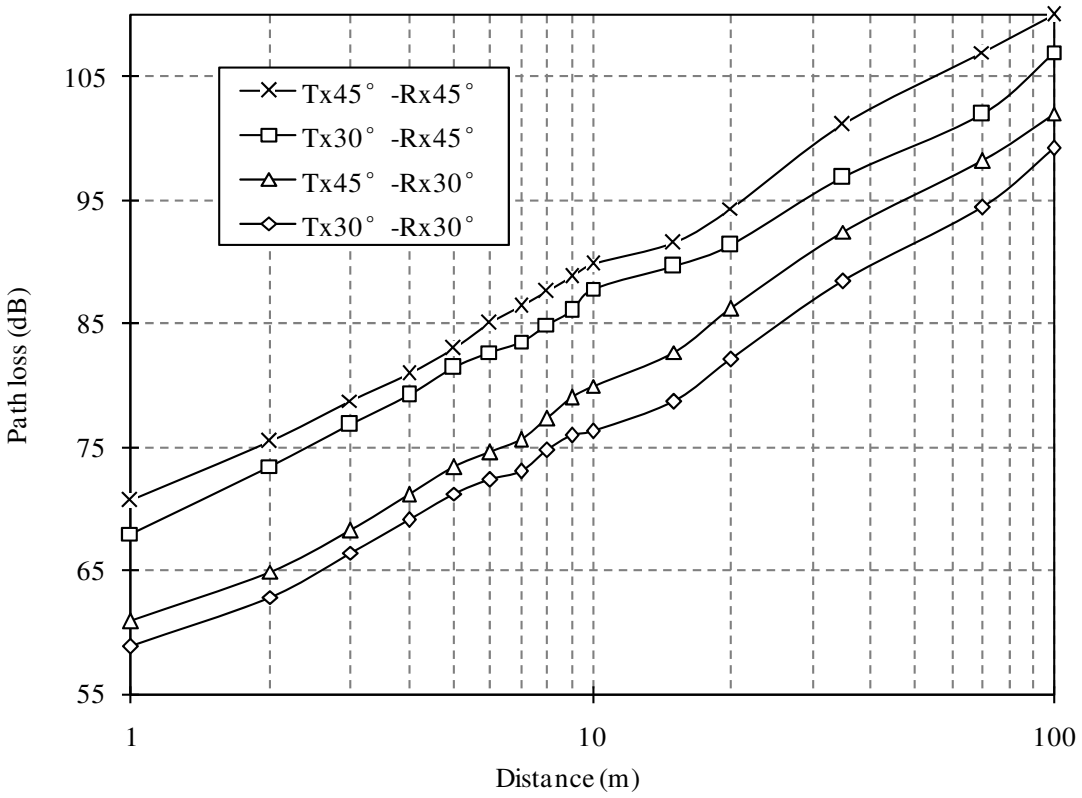

Figure 4.7: Measured path loss for different Tx and Rx elevation angles.

Figure 4.7 from [28] presents path loss versus distance on a logarithmic scale, with each curve parameterized by choice of Tx and Rx elevation angle pairs. We observe that the path loss increases by about 18 dB for each order of magnitude increase in distance r, i.e., path loss is proportional to $r^{1.8}$ under this geometry. However, a path loss exponent of 1.8 is not universal and may change with geometry. For example, for range up to 10 m and Tx/Rx angle of 90^o, the path loss exponent was found to be close to 1.

Figure 4.8 from [37] compares path loss measurement and simulation assuming single scattering. The model parameters matched the experimental measurement system as closely as possible, and assumed a tenuous atmosphere, with the measurements taken outdoors on a clear day. The simulation shows a reasonable agreement, within a few dB. In general, as expected, we observe that the loss increases as either the Tx or Rx angle increases. This is due to the longer propagation path as well as the inherent scattering loss.

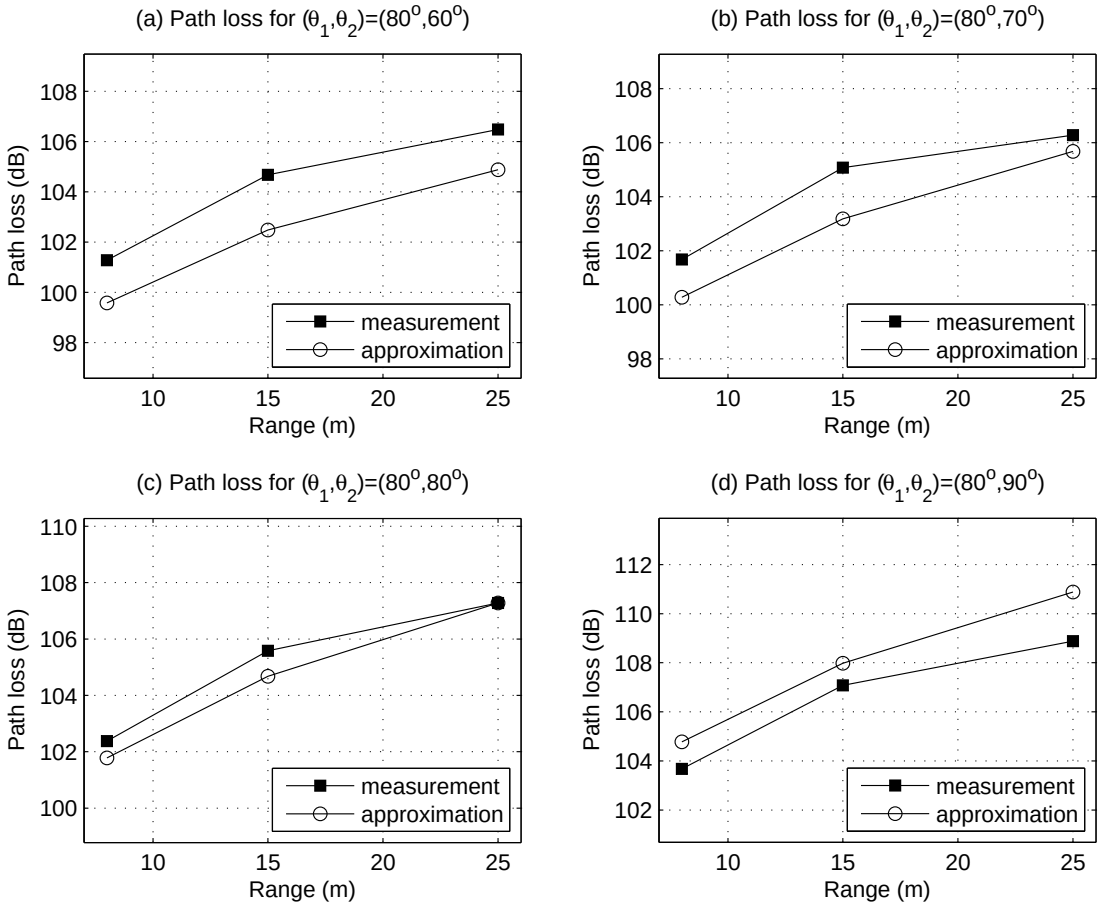

Figure 4.8: Comparison of measured and simulated path loss with four different pointing angle pairs.

A series of impulse response measurements were also obtained, while varying the Tx and Rx elevation angles from 0^o to 90^o, and changing the Tx beam angle, Rx

FOV, and baseline distance up to 100 m. The laser pulse rate was set at 10 Hz, and the output energy after the optical beam shaping system was 3 mJ. Beam divergence was less than 3 mrad, and line width was $1cm^{-1}$. The 270 nm solar blind filter had FWHM bandwidth of 15 nm. The peak transmission was 10.4% at 271 nm, and the out-of-band transmission was less than 10^{-8} at 290 nm, 10^{-10} at 390 nm, and 10^{-11} at $305 \sim 750$ nm. The spectral mismatch between the laser and the filter was found to be less than 30%. The PMT had a circular sensing window with a diameter of 8 mm, and its dark current was 4 nA.

Figure 3.8 from [29] shows typical average impulse responses under different Tx and Rx pointing angles at a range of 100 meters, progressing from a small angle of 10^o to a large angle of 90^o. Each figure corresponds to averaging 50 measured impulse responses. The resulting FWHM pulse width varies from 20 ns to 1500 ns. Note the faster rising edge, followed by slower decay. The decay increases as the elevation angle increases, due to the larger spread in propagation times for scattered photons. With a smaller elevation angle (lower to the horizon), the decay becomes significantly faster and the pulse width is decreased. Note also that, at higher elevation angles (approaching vertical pointing), the responses have more variations from measurement to measurement, and the averaged response continues to exhibit significant fluctuation, even after averaging 50 measurements.

Figure 4.9 compares simulated impulse response with measured response, for four different pointing angle pairs. The pulse spreading is roughly $(200, 300, 400, 500)$ ns for the four pointing geometries indicated in the figure captions. There is a reasonable agreement between the simulation and experimental results. However, other cases have shown larger error between the measurement and simulation, and continued in-

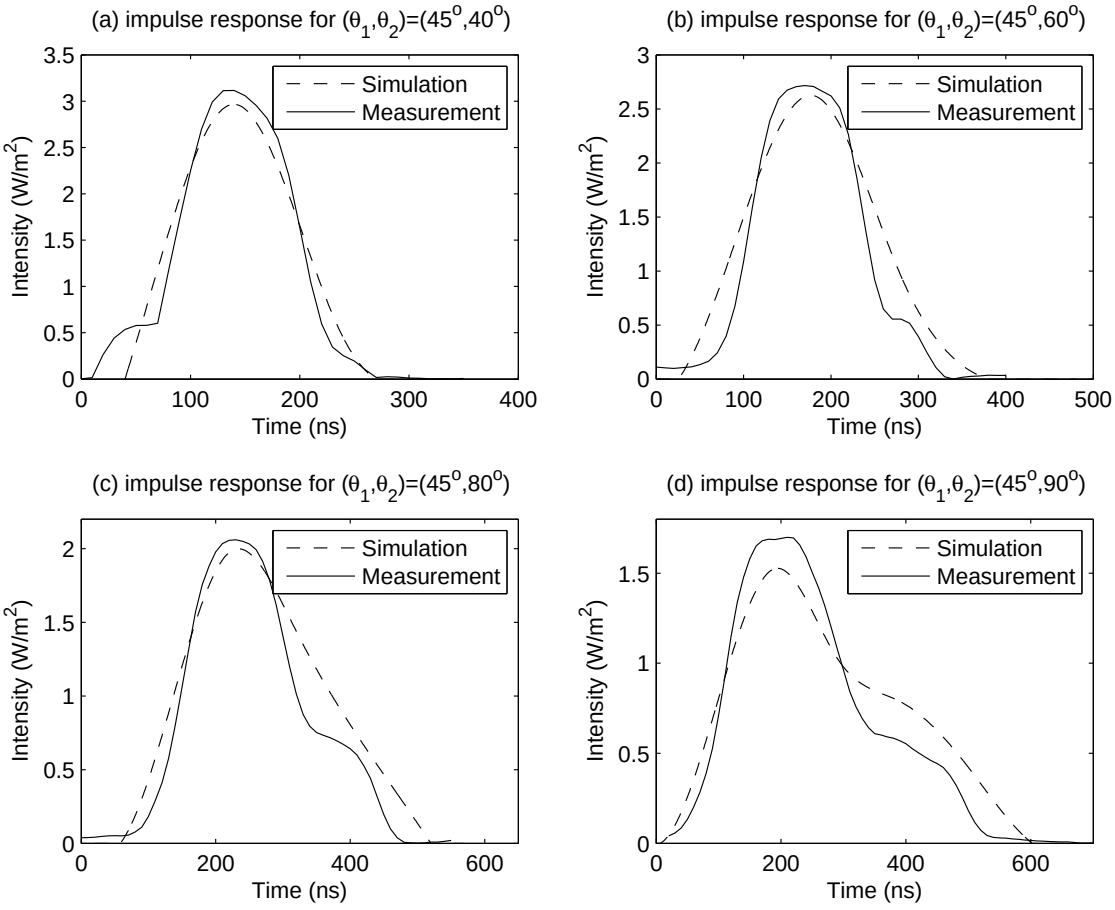

Figure 4.9: Comparison of impulse response simulation with experimental measurement.

vestigation is necessary. We conjecture that some of the mismatch between experiment and prediction can be attributed to system calibration errors, inaccurate atmospheric parameters for the system operating conditions, and other measurement errors.

4.4 UV Link Performance Analysis

In this section, we investigate the NLOS UV link performance by analyzing link path loss, channel bandwidth, data rate and power requirement. All results here are obtained by our simulation method proposed in the previous section.

4.4.1 Simulated Short Range Path Loss

Given experimental LED power limitations, we focus on ranges from 10 meters to 100 meters. Note that path loss is not particularly sensitive to Tx beamwidth angle. We examine the path loss while varying Tx and Rx pointing angles and Rx FOV angle. In our simulations, we assume a default 17^o Tx beam angle, 30^o Rx FOV angle, and 90^o Rx pointing angle unless we explicitly specify these parameters.

Figure 4.10 depicts range-dependent path loss for varying Tx and Rx pointing angles. We can see that path loss is very sensitive to the pointing angles. In particular, for fixed large Tx pointing angles increasing Rx pointing angle may exhibit dramatic path loss deterioration, which implies that it is necessary to increase the transmitted power to compensate the high channel attenuation loss problem for large pointing angle geometry. For example, for fixed transmit power, the NLOS communications range can be extended by lowering the pointing angles towards each other.

Under a solar blind assumption, a wide Rx FOV can increase the received signal power level without a significant increase in noise. We show the FOV effect for path loss in Figure 4.11. Obviously, a wider Rx FOV produces lower path loss as the Rx is able to collect more scattering signal photons. For Tx and Rx pointing angle pair $(60^o, 90^o)$, path loss for 100 meter range shows more than 10 dB improvement by increasing the FOV from 30^o to 180^o. Other geometries also show significant reduction in path loss. However, in some practical scenarios where there is a nontrivial background noise, the FOV needs to be optimized to maximize the receiver SNR and consequently minimize the bit error rate (BER), as described in [46].

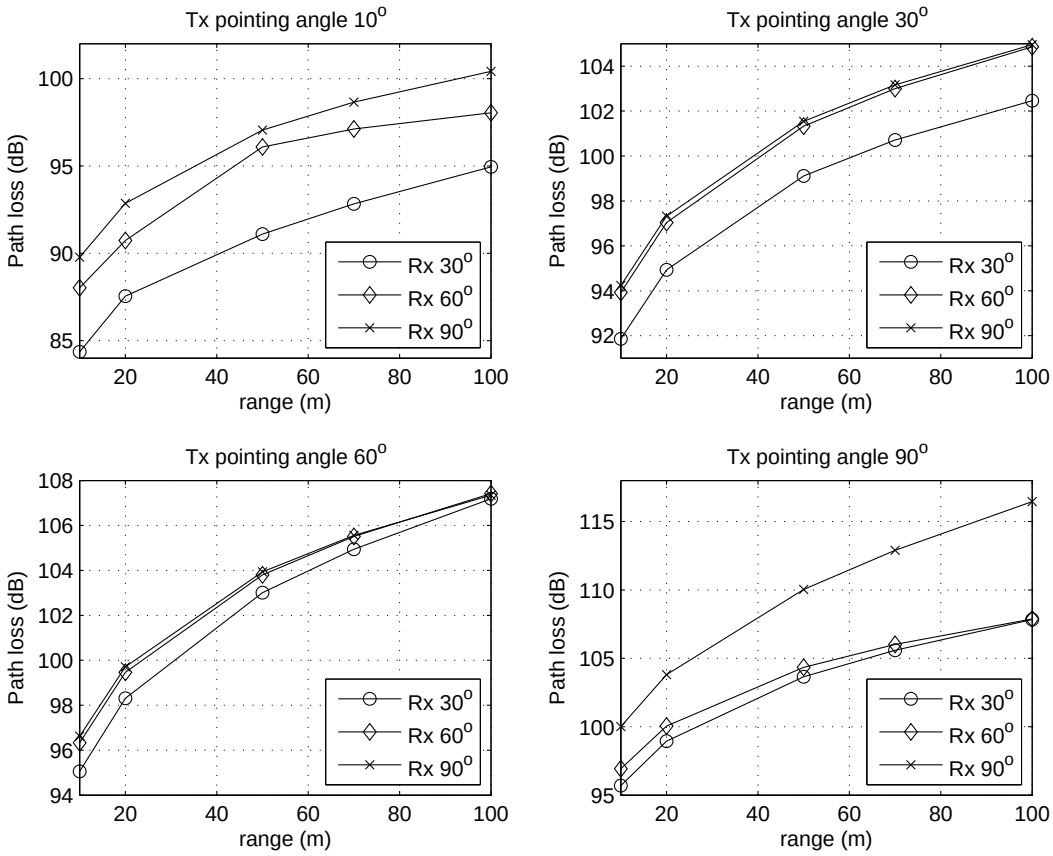

Figure 4.10: Predicted short range path loss for varying pointing angles.

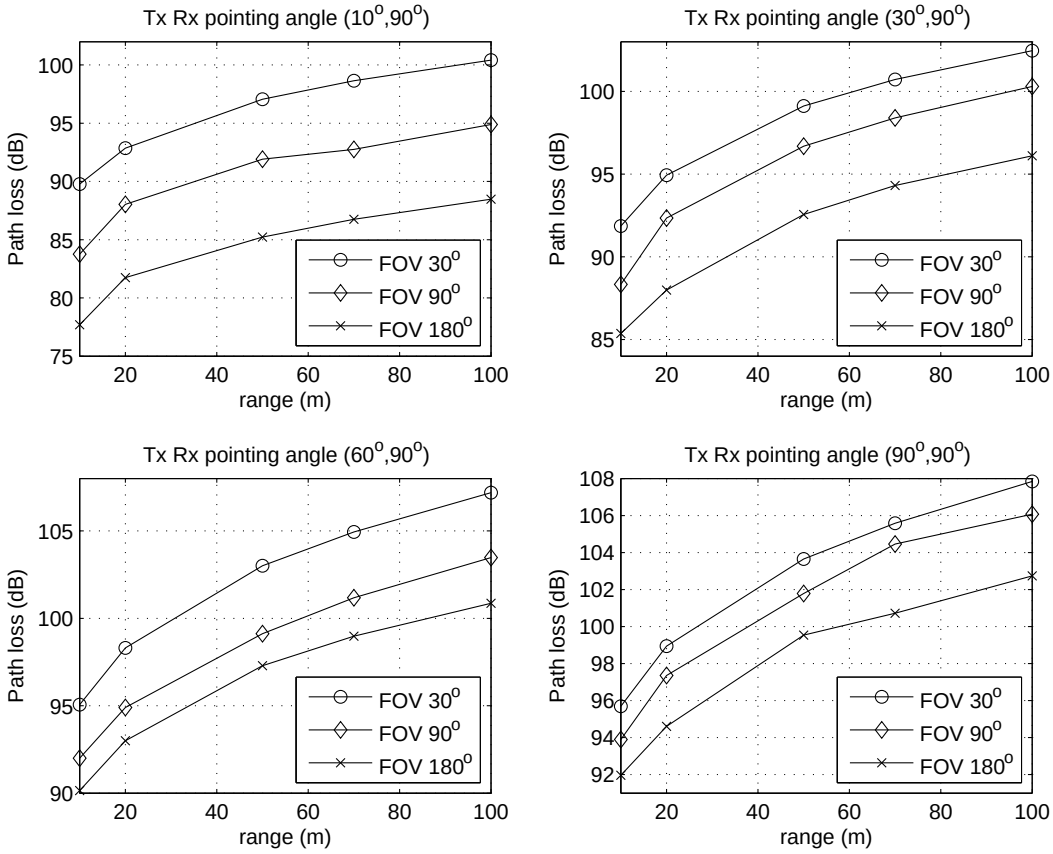

Figure 4.11: Predicted short range path loss for varying FOV angles.

4.4.2 Power-limited or Bandwidth-limited Channel?

We have shown in Figures 4.10 and 4.11 that path loss can be improved by increasing the Rx FOV as well as using small pointing angles for longer range UV links. However, increasing Rx FOV may also generate a loss of bandwidth due to pulse spreading. This occurs as the pointing angles and Rx FOV increase. Although a wide FOV is valuable to combat path loss, it also constrains the bandwidth due to the extended impulse response duration, which leads to a fundamental system tradeoff between path loss and impulse response spreading. The achievable data rate depends not only on the channel bandwidth and path loss, but also many other parameters such as transmitted optical power, background noise, wavelength, and desired BER. Here we study the achievable data rate in two respects. First, we examine the channel 3 dB bandwidth from the simulated impulse response. Then we investigate the data rate which is determined by the transmitted power, desired BER, and link path loss. This reveals whether power or bandwidth is dominant in determining the achievable data rate.

We calculate the 3 dB bandwidth from the simulated channel impulse response. Figure 4.12 depicts range-dependent 3 dB bandwidth for varying Tx and Rx pointing angles. We observe that bandwidth is very sensitive to the pointing angles. In particular, for fixed large Tx pointing angles, increasing Rx pointing angle may result in dramatic bandwidth deterioration, which implies limited achievable data rate for large pointing angle geometry.

Figures 4.12 and 4.13 show the bandwidth determined by impulse response for NLOS UV links. We express the data rate by employing the formulation as described

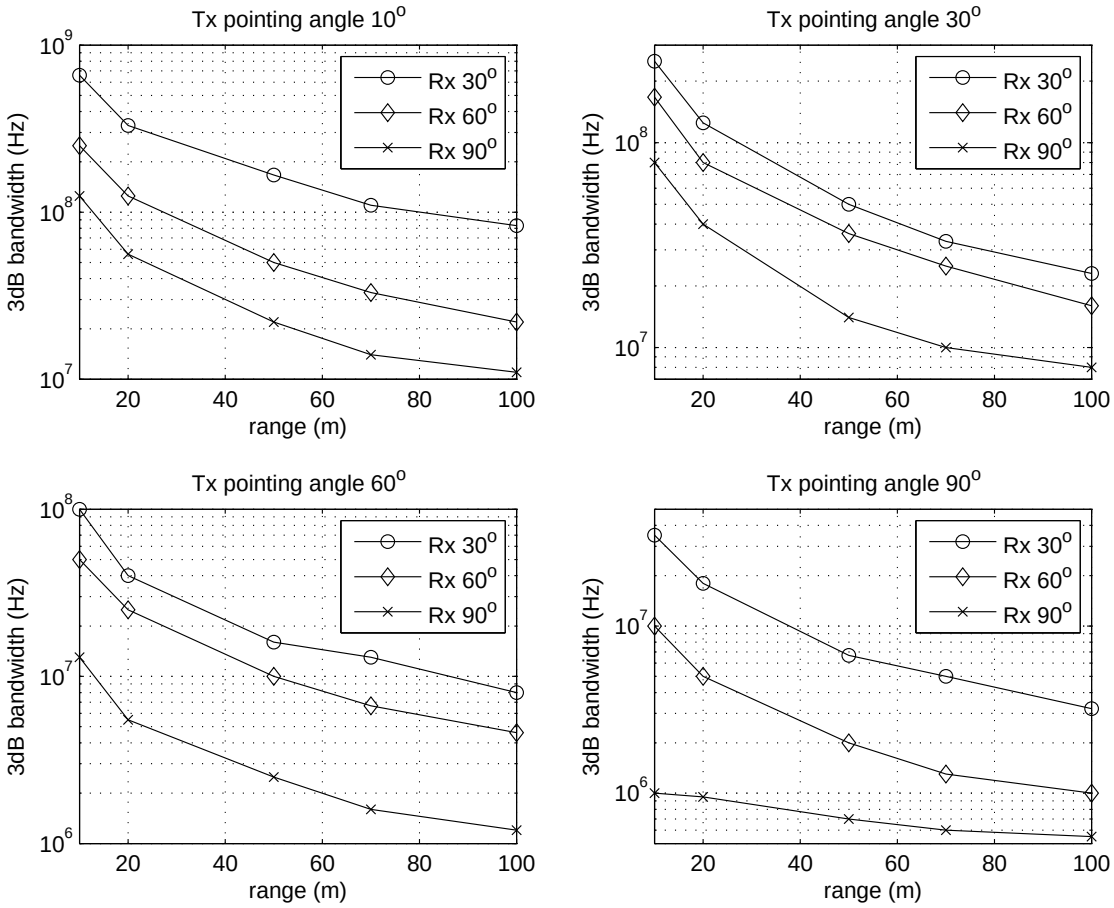

Figure 4.12: Predicted 3dB bandwidth for varying pointing angles.

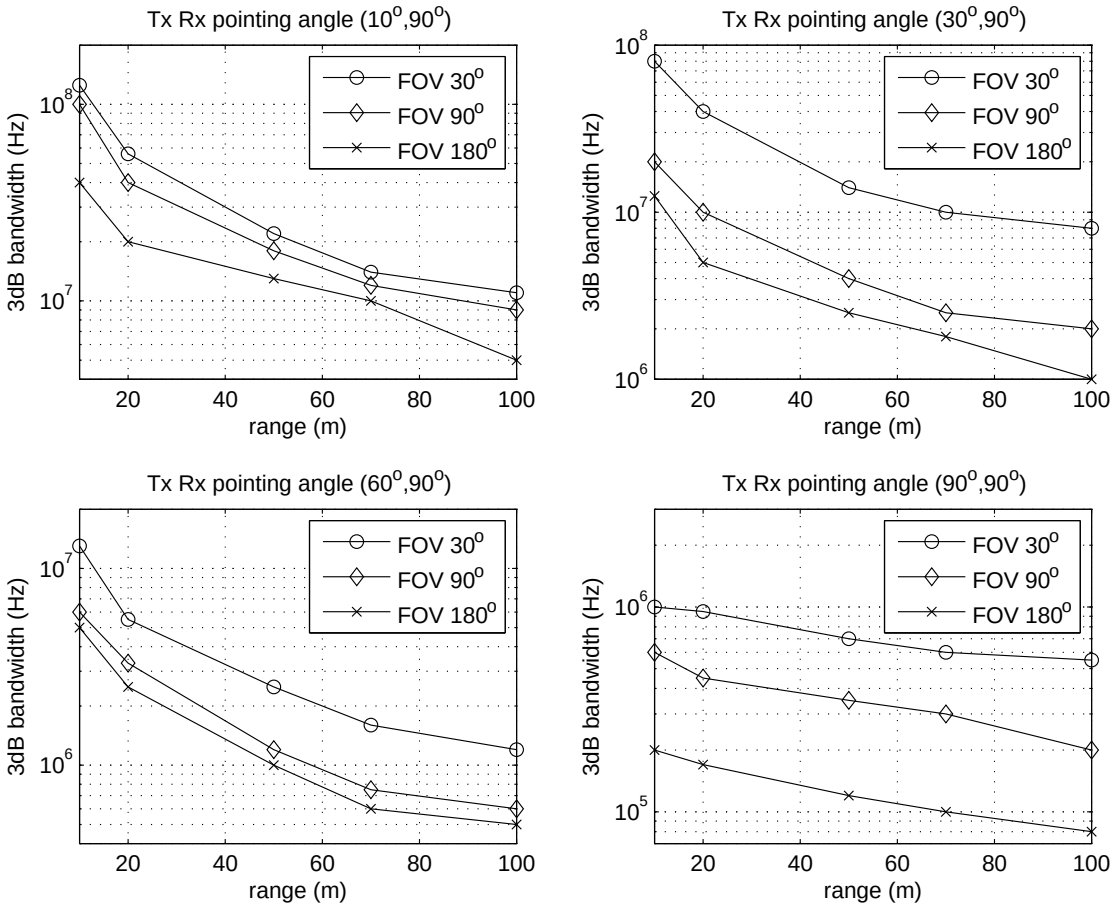

Figure 4.13: Predicted 3dB bandwidth for varying FOV angles.

in [36]

$$R = \frac{\eta_f \eta_r P_t \lambda}{hcLN_d}, \tag{4.27}$$

where R is the data rate, η_f is the filter transmission efficiency, η_r is the Rx detection efficiency, P_t is the transmitted power, λ is the UV wavelength, h is Planck's constant, c is the speed of light, L is the link path loss, and N_d is the number of photons detected per pulse. Our analysis assumes an on-off keying (OOK) modulation and a medium background noise level as in [36]. Given the BER, N_d can be calculated from Equations (4) and (5) in [36]. Using typical experimental values, we assume the following [47]: $\eta_f = 0.2$, $\eta_r = 0.3$, $P_t = 100$mW, $\lambda = 260$nm and BER $= 10^{-3}$. Based on Eq. (4.27), we show the predicted achievable data rate for short ranges by varying pointing angles and Rx FOV in Figures 4.14 and 4.15.

Comparing Figures 4.12 and 4.14, it is evident that the achievable data rate is dominated by path loss, where the corresponding 3dB bandwidth for each geometry is much larger than the data rate result from Eq. (4.27). We have noted that while a wider Rx FOV can decrease path loss and potentially increase data rate, there is a corresponding increase in the pulse spreading. However, from Figures 4.13 and 4.15, we can clearly see that the bandwidth plays a minor role in determining the data rate, because the NLOS UV link based on current system parameters is power limited. For a given set of system parameters, the achievable data rate can be calculated using Eq. (4.27).

4.4.3 Simulated Long Range Path Loss and Power Requirement

The above discussions are for short range NLOS UV communications up to roughly 100 meters. In practical scenarios, longer range communication links (up to

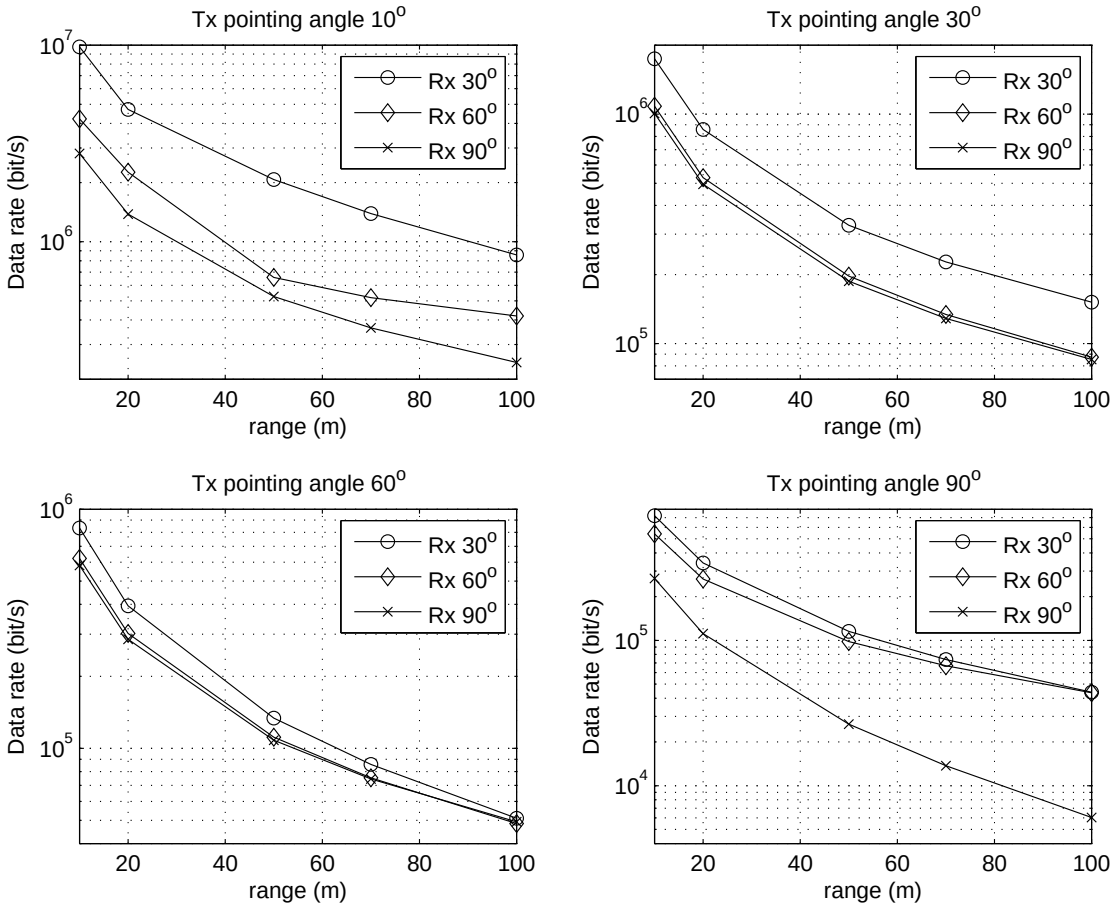

Figure 4.14: Predicted data rate for varying pointing angles.

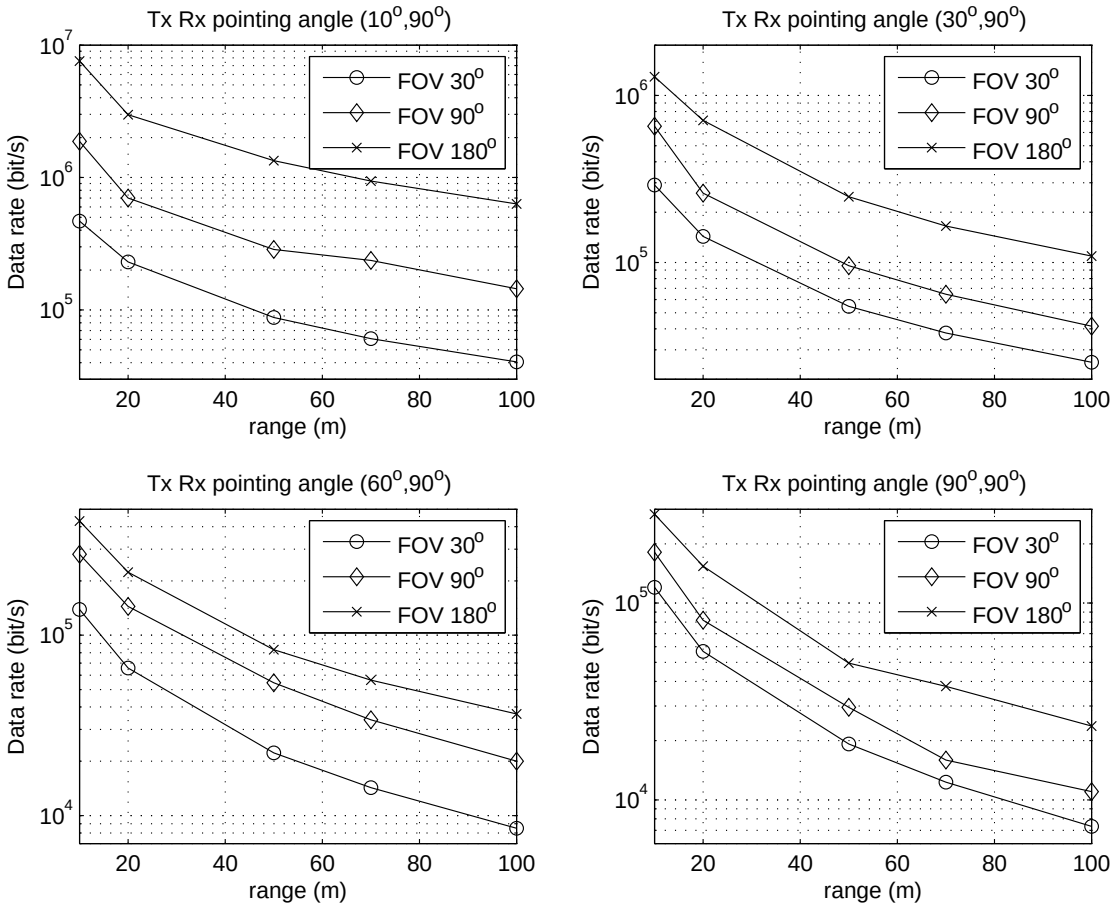

Figure 4.15: Predicted data rate for varying FOV angles.

several kilometers) may also be desired. Although an NLOS UV communication system employing current LED source technology may have a limited communication distance, a higher power UV laser enables a longer communication distance, although eye and skin safety become an issue when exposed to the direct laser beam.

In this subsection, we investigate the power requirement for long-range NLOS UV links by varying system geometry, consider baseline range from 1 kilometer to 5 kilometers, while varying pointing angles and FOV. Both path loss and power requirements are studied. We assume a default 3 mrad Tx beam angle, 30^o Rx FOV angle and 90^o Rx pointing angle unless we otherwise explicitly specify these parameters. Figure 4.16 and 4.17 depict the predicted path loss for varying pointing angles and FOV, respectively. As for short range, we observe that path loss is very sensitive to the pointing angles and FOV. Path loss deteriorates rapidly with increasing pointing angles at long ranges. For example, a path loss of about 180 dB is predicted for pointing angle set $(90^o, 90^o)$ at a range of 5 kilometers, a very large loss that would require a significantly powerful transmitter to overcome. In Figure 4.17, large FOVs result in significant improvements for the link path loss in different geometries. For Tx and Rx pointing angle pair $(60^o, 90^o)$, path loss for a 5 kilometer range shows a 30 dB improvement by changing the FOV from 30^o to 180^o, although this assumes the background noise count is not increasing with enhanced FOV and ultimately it may be desirable to find a good tradeoff in Rx FOV as we noted earlier.

Figures 4.16 and 4.17 demonstrate very large path loss results for long range links, demonstrating that at longer ranges the NLOS UV link is very much power limited. Here we further study the power requirement for long range UV links. For given system

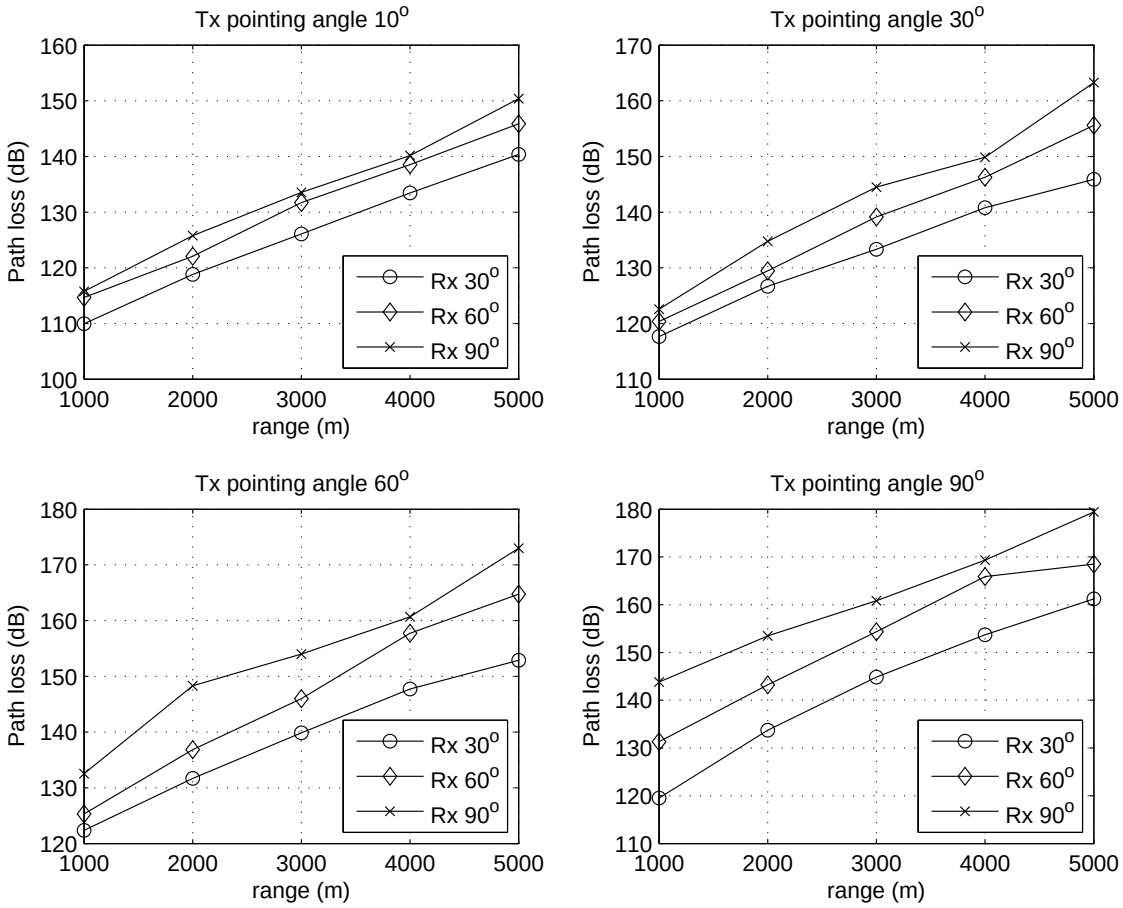

Figure 4.16: Predicted long range path loss for varying pointing angles.

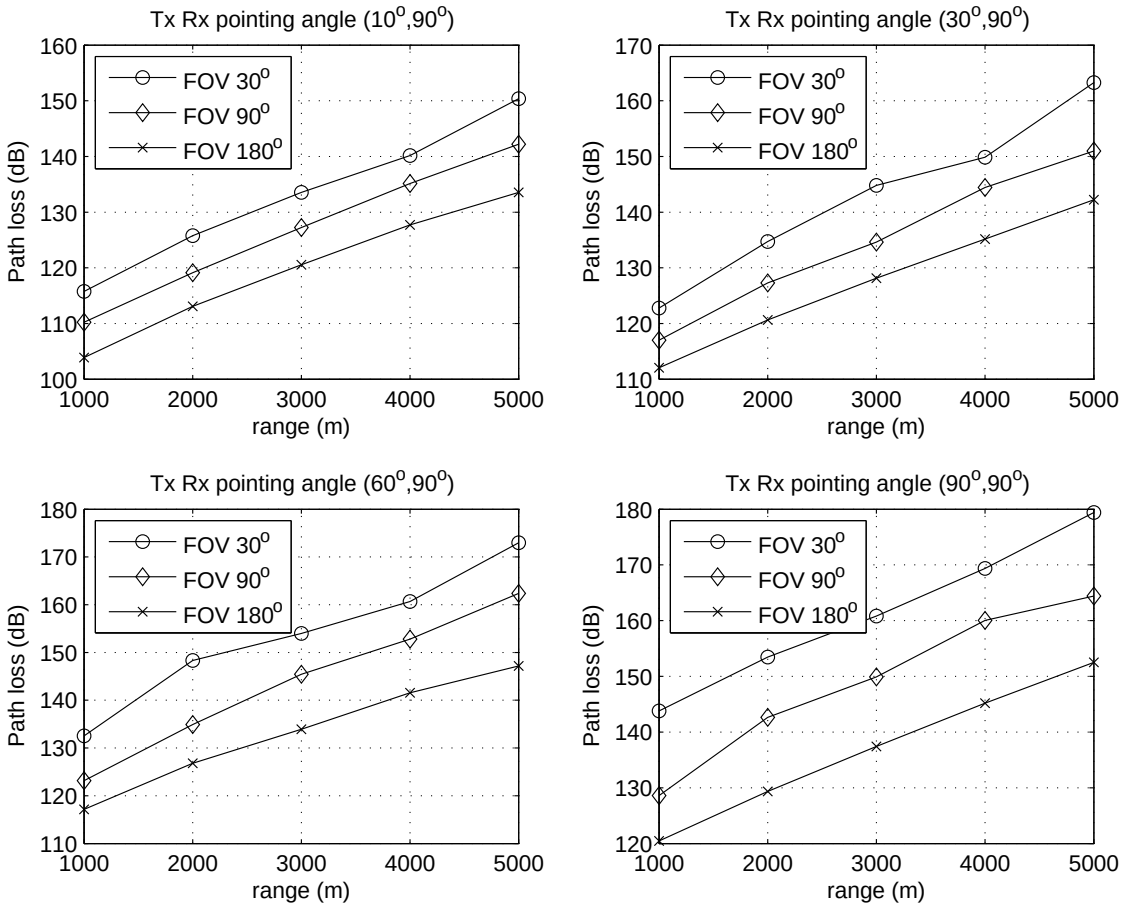

Figure 4.17: Predicted long range path loss for varying FOV angles.

parameters, we can derive the required transmission power from Eq. (4.27) to be

$$P_t = \frac{RhcLN_d}{\eta_f \eta_r \lambda}. \tag{4.28}$$

From Eq. (4.28), for fixed system parameters, we observe a linear relationship between transmitted power and path loss. For example, assuming the following parameters, $\eta_f = 0.2$, $\eta_r = 0.3$, $R = 5kbps$, $\lambda = 260nm$ and $BER = 10^{-3}$, we obtain $P_t = 1.8704 \times 10^{-13} L$. Here we define path loss $L = P_t/P_r$, where P_t and P_r are transmitted power and received power, respectively. Based on the linear relationship, we can predict similar results for power requirement with varying geometry. This quickly yields practical limitations on NLOS UV links. For example, for a $(90^o, 90^o)$ pointing angle link at a range of 5 kilometers, we may need more than 10^5 watt power to achieve $BER = 10^{-3}$ and $R = 5kbps$.

4.5 NLOS UV Turbulence Analysis

Scattering and absorption effects have been studied and modeled for UV NLOS links [37],[41], [45], while turbulence is generally ignored at relatively short ranges and clear weather conditions. However, optical turbulence effects in UV band may degrade communication link performance as distance is extended, including irradiance fluctuation (scintillation) and beam wander [1],[30],[48]. For NLOS UV links, irradiance fluctuation can be a limiting factor for systems operating in various turbulence environments. Optical turbulence has been investigated via field measurements and wave propagation theory [49],[50]. For example, the irradiance fluctuation has been modeled using a log-normal distribution for weak atmosphere turbulence conditions [48],[49],[51]. However, the existing measurements and analysis are typically based on a line-of-sight scenario such that the optical Tx and Rx point to each other directly. To the best of

our knowledge, turbulence has not been studied in the context of NLOS links. Here, we propose an irradiance fluctuation model for NLOS UV communications. As we noted, NLOS UV communication system performance has been evaluated for short range links (up to several hundred meters) [28],[29]. For longer range (several kilometers) NLOS UV links, irradiance fading may significantly affect the received signal. According to the Rytov solution to the wave equation, the log-amplitude variance is proportional to the -7/6 power of the wavelength. This implies, for example, that the irradiance fluctuation due to atmospheric turbulence can be two or three times greater in the UV than in the visible, implying that UV links should be more sensitive to turbulence than in the visible.

In this section, we develop an irradiance fluctuation distribution model for NLOS UV links. Our turbulence investigation is based on existing LOS turbulence theory applied to two LOS links from single scattering modeling: from the Tx to the beam/FOV common volume and common volume to the Rx. We expand current models by considering the scattering effects for NLOS scenarios. A model for the received signal distribution is derived, and this is applied to predict system performance.

4.5.1 LOS UV Optical Turbulence and Scintillation

Optical turbulence is the result of random changes in the atmospheres refractive index. This follows from random fluctuations in the atmosphere's temperature generating random irregularities in the index of refraction. Upon passing through these irregularities, an optical wave will be distorted, with the magnitude of the distortions depending on the strength of the turbulence and the length of the optical path. An approximation relating the index of refraction and the atmosphere temperature is given

by [6]

$$n \approx 1 + 77.6\frac{P}{T}[1 + 7.52 \times 10^{-3}\lambda^{-2}] \times 10^{-6}, \tag{4.29}$$

where P is the air pressure in millibars, T is the temperature in Kelvin, and λ is the wavelength in microns.

Corresponding variations in the atmosphere temperature are transported by naturally occurring random fluctuation in wind velocity. These variations then induce the random fluctuations in the atmosphere index of refraction. In the literature, the index of refraction is defined as the sum of its free space value plus a random fluctuating component due to the presence of turbulence

$$n(\mathbf{r}, t) = 1 + n_1(\mathbf{r}, t) \tag{4.30}$$

where $n_1(\mathbf{r}, t)$ is the fluctuating component and it is a function of position $\mathbf{r}$ within the atmosphere and time t.

Due to the random nature of optical turbulence, it is represented in statistical quantities. The two basic statistical parameters are the structure function and the correlation function of the index of refraction

$$D_n(\mathbf{r_1}, \mathbf{r_2}) = E[(n(\mathbf{r_1}) - n(\mathbf{r_2}))^2], \tag{4.31}$$

$$\Gamma_n(\mathbf{r_1}, \mathbf{r_2}) = E[n(\mathbf{r_1})n(\mathbf{r_2})], \tag{4.32}$$

where E[ ] notation denotes an expected value.

From Kolmogorov's theory, the power spectral density is defined as the three-dimensional Fourier transform of the refractive index correlation. The power spectral density is given by

$$\Phi(K) = 0.033C_n^2K^{-11/3} \tag{4.33}$$

where C_n^2 is the index of refraction structure parameter, and K is the vector wavenumber. The value of C_n^2 is altitude dependent. Fried proposed an analytical model for C_n^2 by fitting the data given by Hufnagel and Stanley [6]

$$C_n^2(z) = K_0 z^{-1/3} e^{-\frac{z}{z_0}}, \tag{4.34}$$

where K_0 is the turbulence strength parameter with units of $m^{-2/3}$, and z is the altitude in meters. For a near ground scenario, C_n^2 is typically varying from $1 \times 10^{-13} m^{-2/3}$ for strong turbulence to $1 \times 10^{-17} m^{-2/3}$ for weak turbulence. For weak optical turbulence, the Rytov solution to the wave equation describes scintillation in terms of the variance in log-amplitude of the received wave. The variance of the log amplitude fluctuation X over channel length L for a plane wave is given by [6]

$$\sigma_X^2(L) = 0.56(\frac{2\pi}{\lambda})^{7/6} \int_0^L C_n^2(x)(L-x)^{5/6} dx, \tag{4.35}$$

and for a spherical wave

$$\sigma_X^2(L) = 0.56(\frac{2\pi}{\lambda})^{7/6} \int_0^L C_n^2(x)(\frac{x}{L})^(5/6)(L-x)^{5/6} dx. \tag{4.36}$$

The variance of the irradiance fluctuation predicted by Rytov theory is then given by [6]

$$\sigma_I^2 = e^{4\sigma_x^2} - 1. \tag{4.37}$$

where σ_I^2 is sometimes also named as scintillation index.

The probability distribution function (PDF) of irradiance fluctuation $f(I)$ caused by weak turbulence has been well represented by a log-normal (LN) distribution. For strong turbulence conditions, Churnside and Hill showed that log-normal distribution may be still true if a sufficiently large receiver aperture is used. Bernhard [51] also proposed a simplified free space channel model by applying the LN PDF to

model the optical turbulence. In this paper, we will deploy the LN PDF in LOS scenario and expand it to the NLOS turbulence analysis. The normalized LN PDF of the received irradiance fluctuation is given by

$$f(I) = \frac{1}{I\sigma_I\sqrt{2\pi}} e^{-\frac{(ln\frac{I}{E[I]}+\frac{1}{2}\sigma_I^2)^2}{2\sigma_I^2}}. \tag{4.38}$$

During the analysis described for the received irradiance fluctuation in subsection, the above LN PDF is used as the basis for NLOS scenarios. We will explore the irradiance distribution for NLOS UV scattering channel to propose an analytical distribution modeling method.

4.5.2 NLOS UV Scintillation Model

As discussed above, the NLOS UV channel involves a variety of phenomena, including molecular scattering and absorption, aerosol scattering and absorption, and atmospheric turbulence. The scattering of light occurs because of the presence of the suspended particulates in the atmosphere. For NLOS UV communication, scattering serves as the vehicle for information exchange between the Tx and Rx. Absorption will attenuate the signal during transmission in the atmosphere. Turbulence will cause fluctuation fading for the received signal. However, all the existing models and analysis for NLOS UV ignore the atmosphere effect. We propose an initiative NLOS UV turbulence distribution model in this section based on a typical communication geometry [4], as shown in Figure 2.2.

The weak atmosphere turbulence of LOS UV radiation was measured and analyzed by Daniel and David [50]. Their work measured the UV (254 nm) scintillation index σ_I^2 (up to 0.4) and turbulence structure parameter C_n^2 for a baseline separation of 185 meters. They also validated their measured density distribution of received signal

as LN PDF. Their measured weak turbulence structure parameters C_n^2 for the daytime varies from $1\times10^{-13}m^{-2/3}$ to $5\times10^{-13}m^{-2/3}$, however, traditional measured results define weak turbulence as C_n^2 less than $1\times10^{-17}m^{-2/3}$, and strong turbulence as C_n^2 larger than $1\times10^{-13}m^{-2/3}$. For our following study, we will vary C_n^2 from $1\times10^{-13}m^{-2/3}$ to $1\times10^{-17}m^{-2/3}$ to investigate clearly and completely.

For NLOS UV geometry in Figure 2.2, if atmosphere turbulence occurs, we cannot directly conclude that the received signal will follow the distribution as in the LOS scenario. However, we may still utilize the LOS turbulence model because we may view the NLOS geometry as configured by two LOS paths: one is from Tx to common volume, and the other is from common volume to Rx. For each path, under certain assumptions, we can use the previous distribution to model the turbulence and then combine the two LOS results to obtain the NLOS signal distribution under turbulence. We assume that the Tx beam is small enough so that the common volume can be analytically approximated and signal intensity within the common volume is constant (corresponding to small common volume). We also assume that only single scattering dominates the received signal. Assume unit power is emitted at the Tx. We can calculate the average power in common volume and the received power at the Rx without turbulence [37]. Adding the atmosphere turbulence as discussed in the previous section, the arrival power at common volume has a LN PDF given by

$$f_x(x)=\frac{1}{x\sigma_x\sqrt{2\pi}}e^{-\frac{(ln\frac{x}{E[x]}+\frac{1}{2}\sigma_x^2)^2}{2\sigma_x^2}}, \tag{4.39}$$

where x represents the power level in the common volume, σ_x^2 can be calculated based on Eq. (4.37).

Correspondingly, the conditional arrival power level (y) at the Rx is given by

$$f_y(y|x)=\frac{1}{y\sigma_y\sqrt{2\pi}}e^{-\frac{(ln\frac{y}{E[y|x]}+\frac{1}{2}\sigma_y^2)^2}{2\sigma_y^2}}, \quad E[y|x]=xA, \tag{4.40}$$

where $A = \frac{A_r e^{-k_e r_2}}{r_2^2}$ is a scalar for a fixed NLOS geometry and A_r is the area of detector, σ_y can also be calculated by Eq. (4.37). Thus, the joint PDF of x and y can be derived by

$$f_{x,y}(x,y) = f_y(y|x) f_x(x). \tag{4.41}$$

Therefore, we can represent the PDF of y as

$$f_y(y) = \int f_{x,y}(x,y) dx. \tag{4.42}$$

The above derivation is based on the assumption that the scintillation in common volume is constant for a fixed geometry. We formulize the received signal distribution at the Rx in a NLOS UV scenario in Eq. (4.42). Due to complex integration, there is no clear clue about the exact scintillation distribution in the NLOS UV case. Next we will gain some insight from numerical case study.

4.5.3 NLOS UV Turbulence Case Study

We employ the UV laser's specifications in our experimental setup [29] with beam divergence of 3 mrad, and use atmospheric coefficients at wavelength 260 nm given by $k_s^{Ray} = 0.266 m^{-1}$, $k_s^{Mie} = 0.284 m^{-1}$, and absorption coefficient $k_a = 0.802 m^{-1}$. To be consistent with our experimental conditions, we set the geometric and model simulation parameters as follows: $(\phi_1, \phi_2, \theta_1, \theta_2) = (3mrad, 30^o, 30^o, 30^o)$, r=100m, and the receiver area is $1.77 cm^2$, $C_n^2 = 1 \times 10^{-13} m^{-2/3}$. We will use this default configuration unless otherwise specification.

We assume that plane wave is transmitted by a UV laser, thus we can calculate the irradiance variances for the two separated LOS paths respectively. From the derivation above, we can calculate the LOS signal distribution, conditional signal distribution, and then obtain the NLOS signal distribution in Eq. (4.42). We further deploy the

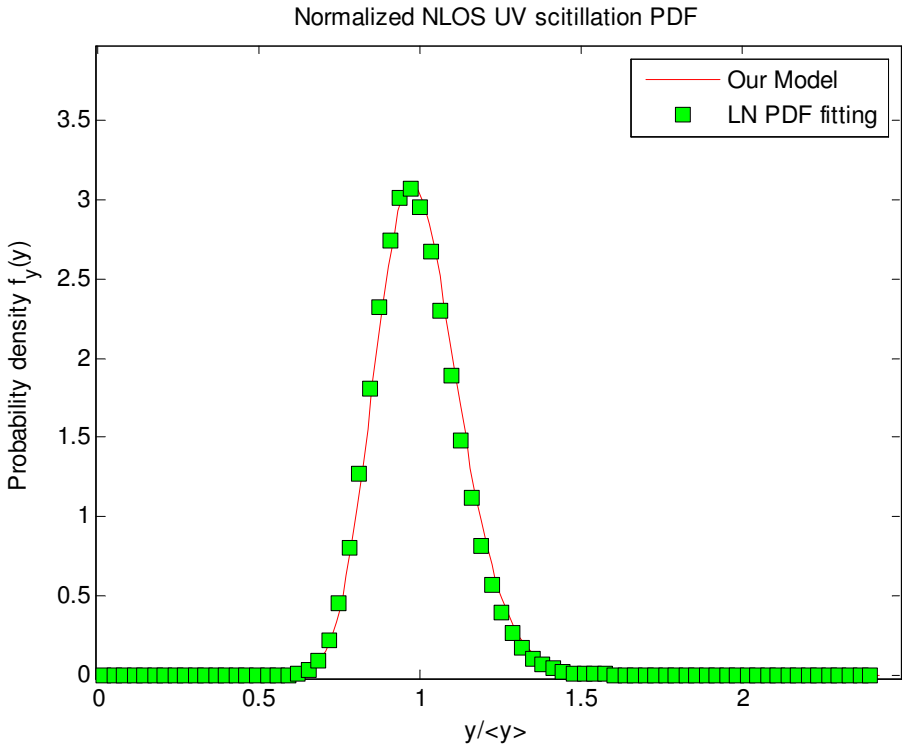

Figure 4.18: Probability density function of NLOS UV scintillation.

LN PDF to fit the calculated model. Figure 4.18 shows the analytical distribution by comparing it with the fitting LN PDF. We find that the goodness-of-fit is satisfactory. Our proposed distribution model for NLOS UV scenario is well fitted by the LN PDF for this specific case.

Next, we evaluate the received signal distribution by varying the optical pointing angles, atmosphere structure parameters, and baseline separation range.

Figure 4.19 shows the received signal PDFs with four pointing angle pairs. We limit the largest pointing angles to $(60^o, 60^o)$ to ensure that the common volume is small and the assumptions in the derivation reasonable. Also shown for comparison are curves from LN PDF fitting, which is a good fit for all four cases. The predicted NLOS scintillation index increases with pointing angle. In this scenario, we obtain $\sigma_I^2 = 0.0483$

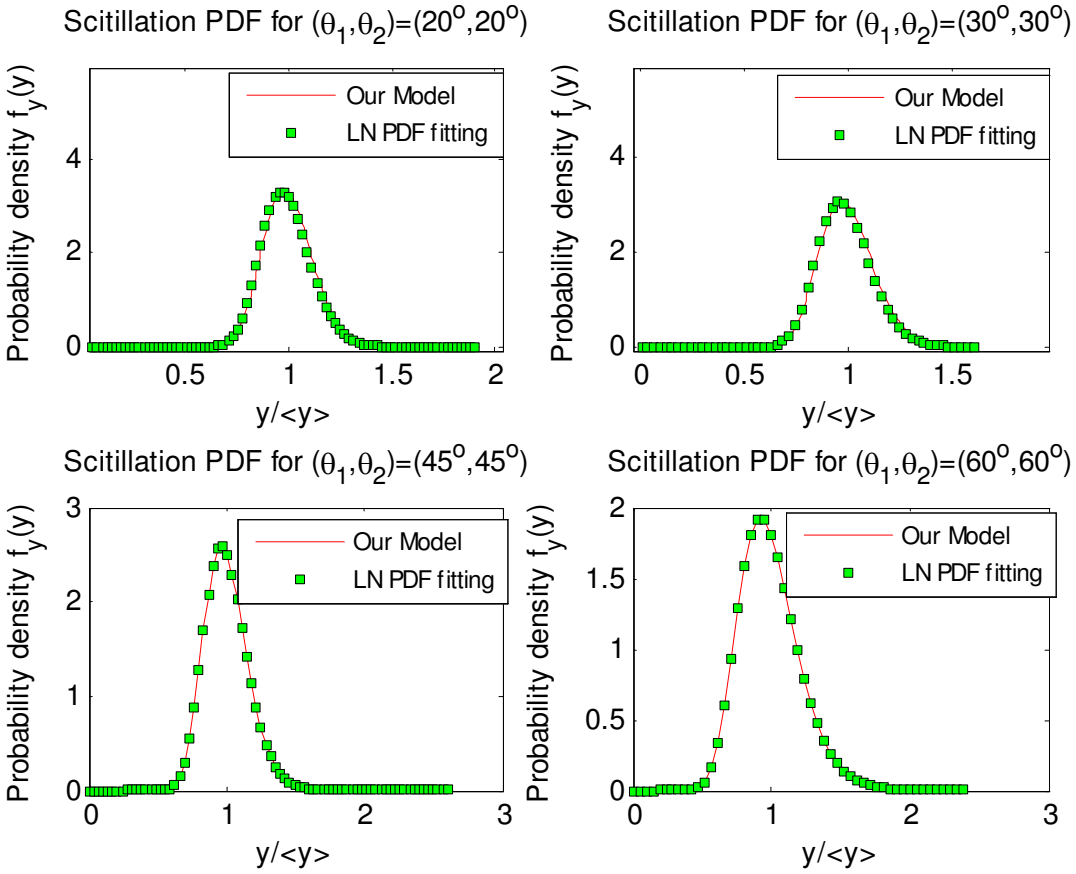

Figure 4.19: PDF of NLOS UV scintillation for varying pointing angles.

for the pointing angle pair $(\theta_1, \theta_2) = (60^o, 60^o)$, and smaller scintillation index occurs for smaller pointing angles.

Next we vary the atmosphere structure parameters using typical values for different atmospheric conditions. Figure 4.20 illustrates the scintillation PDFs for the corresponding different turbulence conditions. A large NLOS scintillation index ($\sigma_I^2 = 0.1945$) is calculated for $C_n^2 = 1e^{-13}$, and an extremely small NLOS scintillation index ($\sigma_I^2 = 0.00017$) is obtained for $C_n^2 = 1e^{-16}$. These predicted results agree with the LOS turbulence definition for weak and strong turbulence mentioned previously. Stronger scintillation is predicted with a larger atmosphere structure parameter in a NLOS UV

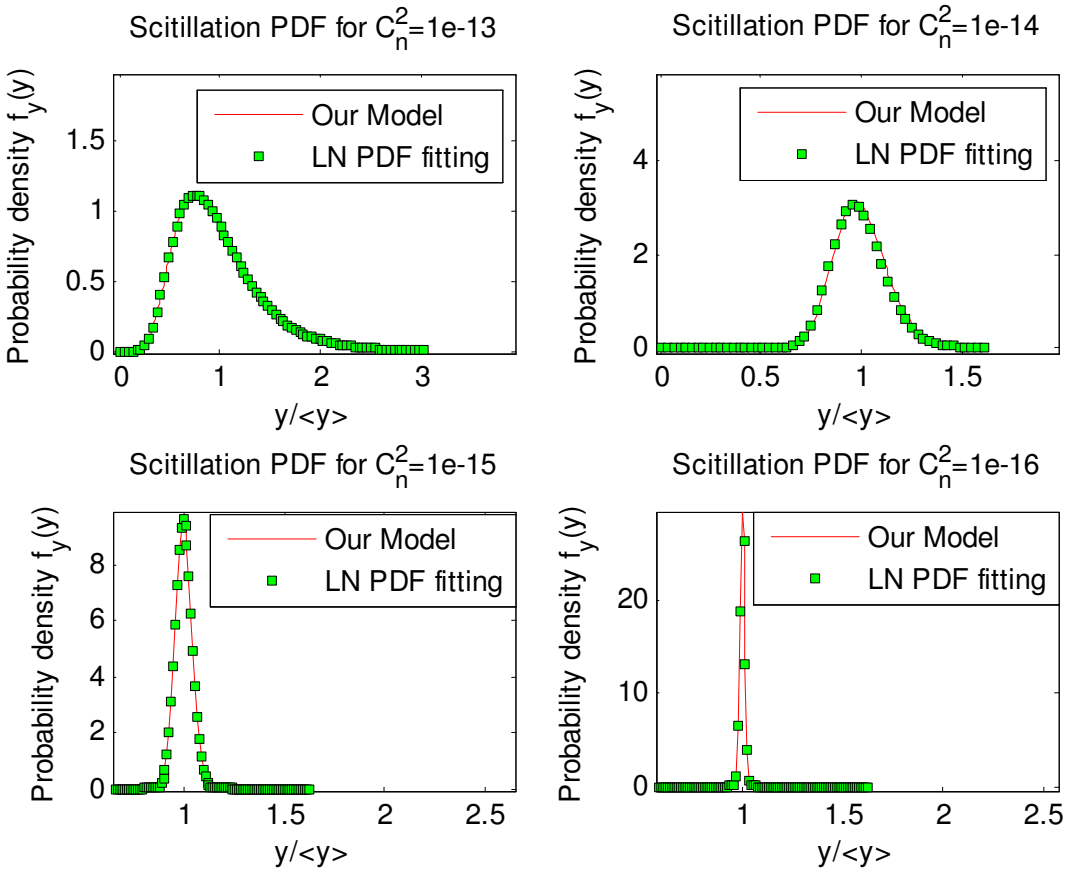

Figure 4.20: PDF of NLOS UV scintillation with varying atmospheric structure parameter.

links.

Figure 4.21 depicts the scintillation PDFs for NLOS UV links with varying baseline range. We limit the baseline range to 1000m to apply the corresponding approximations. The predicted scintillation index increases greatly (from 0.0172 to 3.82) as we change the baseline range from 100m to 1000m. This implies that fading mitigation techniques are needed for a large NLOS link distance (several kilometers) scenario where atmosphere scintillation may cause serious temporal and spatial fluctuation of the received signal.

The bit-error-rate (BER) for a NLOS UV communication system depends on

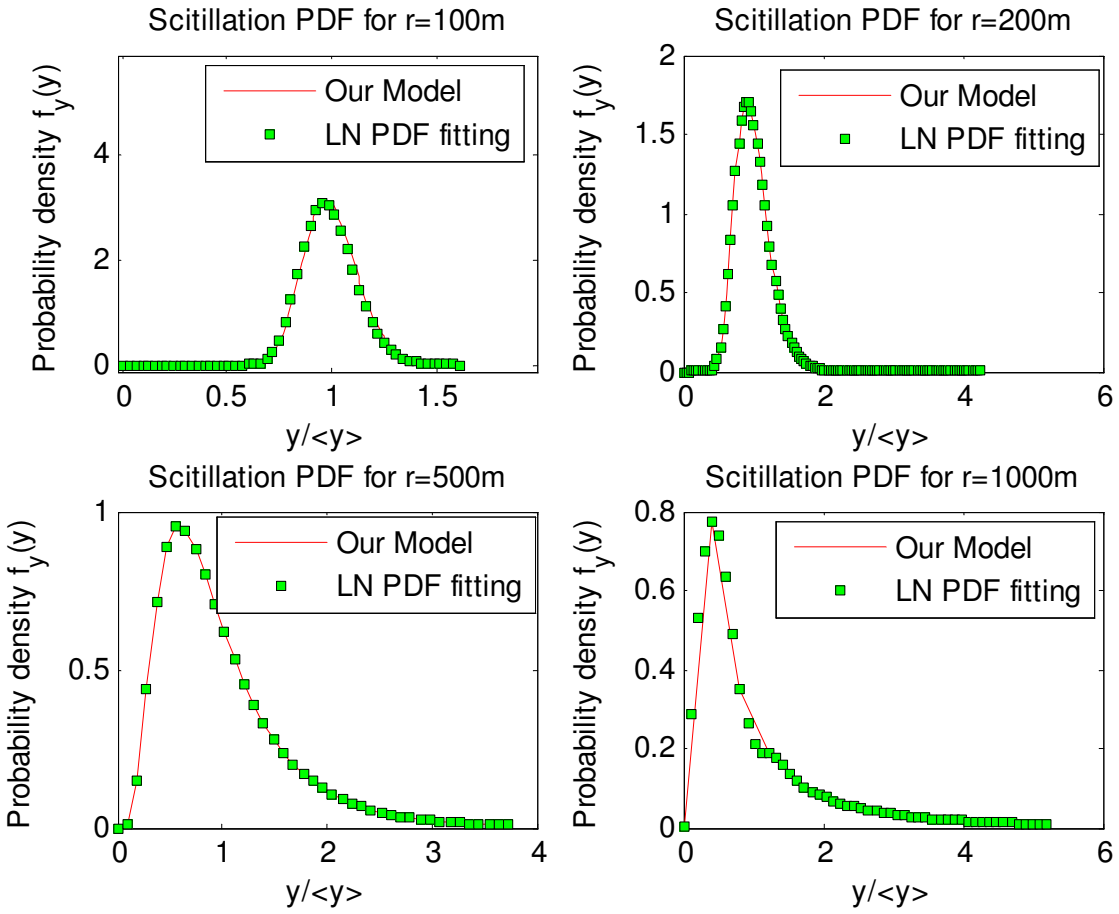

Figure 4.21: PDF of NLOS UV scintillation with varying baseline range.

several parameters, including modulation format, detector type, transmitted power, path loss, scintillation, data rate and noise4. We restrict our attention to on-off keying (OOK) with direct detection, and analyze BER performance of the corresponding NLOS UV. In the NLOS UV link with atmospheric turbulence, the received signal may experience additional losses and random irradiance fluctuations. The mean quantum-limit based signal-to-noise ratio (SNR) in the case of turbulence is given by [48]

$$< SNR_{T,NLOS} >= \frac{SNR_{0,NLOS}}{\sqrt{\frac{P_{ro}}{P_r} + \sigma_y^2 SNR_{0,NLOS}}}, \tag{4.43}$$

where P_{ro} is the received power without turbulence, $< P_r >$ is the mean received power with turbulence, and $SNR_{0,NLOS}$ is the SNR in a NLOS communication link assuming no turbulence. To simplify our analysis, we assume that P_{ro} equals $< P_r >$, and $SNR_{0,NLOS} = \sqrt{\frac{y_0}{2Rhc/\lambda}}$, where y_0 is the received power without turbulence and can be obtained from the single scattering approximation, R is the link data rate, h denotes Planck constant, c is the speed of light, and λ is the wavelength.

In the presence of turbulence, the BER is calculated from the conditional probability that is averaged over the PDF of the random signal. The turbulence based BER is then represented by [48]

$$BER_{T,NLOS} = \frac{1}{2}\int_0^\infty f_y(y) erfc(\frac{< SNR_{T,NLOS} > y}{2\sqrt{2}})dy \tag{4.44}$$

To study the turbulence effect on a NLOS UV link performance quantitatively, we assume the above default parameters. Other parameters are set as: $R = 5kbps$, $c = 3 \times 10^8 m/s$, and $h = 6.62606896 \times 10^{-34}$. We apply the NLOS UV scintillation PDF derived as above and plot BER performance predicted in Eq. (4.44).

Figure 4.22 predicts that the BER will increase almost linearly from 1×10^{-4} to about 0.02 as (θ_1, θ_2) increases from $(20^o, 20^o)$ to $(60^o, 60^o)$. Figure 4.23 predicts rapid BER degradation with increasing baseline range, here varying from 2.84×10^{-4} to 0.2466

when the baseline range changes from 100 to 1000 meters. Our calculations also show that the BER is very sensitive to the atmosphere structure parameter. For example, for atmospheric and geometry parameters (θ_1, θ_2)=$(30^o, 30^o)$, r=100m, $C_n^2 = 1 \times 10^{-16}$, the BER is so small that turbulence may have little influence for the NLOS UV link.

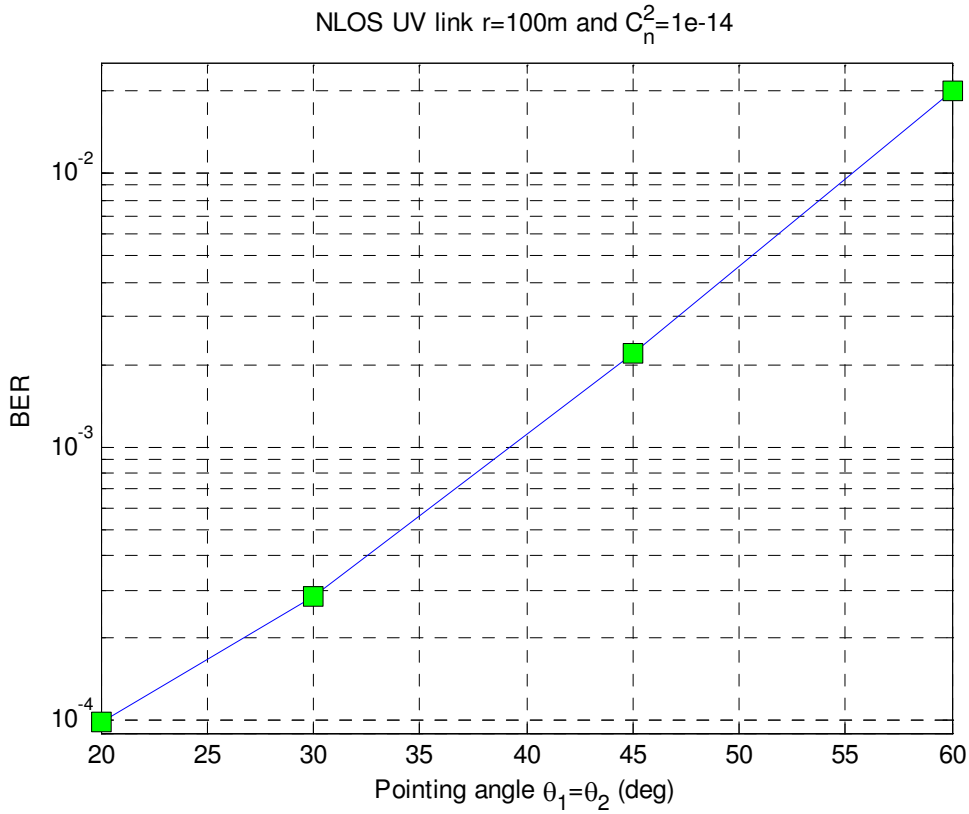

Figure 4.22: BER versus pointing angle in a turbulent NLOS UV link.

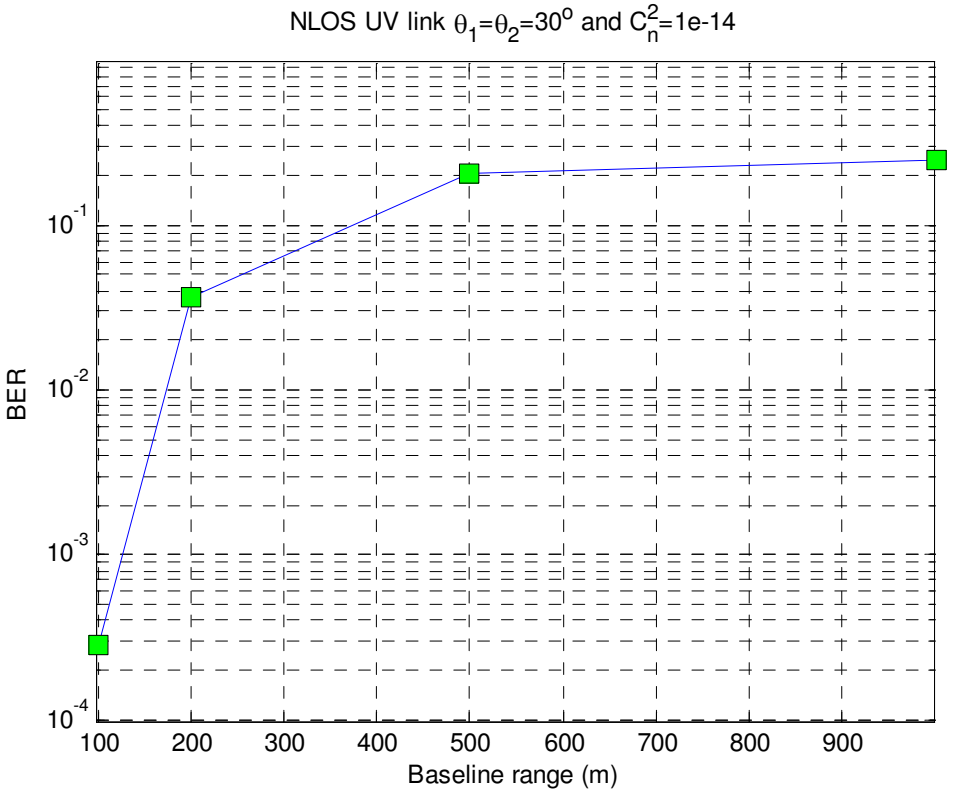

Figure 4.23: BER versus baseline range in a turbulent NLOS UV link.

Chapter 5

Conclusions

In a NLOS communication scenario, solar blind UV signals suffer from extinction due to atmosphere absorption and scattering. This thesis focused on NLOS UV scattering channel characterization and modeling, especially NLOS UV channel impulse response and path loss modeling, and analyzed the UV link performance for short ranges. The single scattering and multiple scattering effects were included for cases of applicability.

A NLOS UV single scattering channel model was parameterized and approximated for simplicity and tractability. Multiple scattering models were further analytically developed by simulating a complex process as a succession of elementary events whose probability laws were known. The closed-form expression of multiple scattering path loss enables easy study of higher order scattering effects. NLOS UV channel measurements were conducted extensively for varying geometries through our UV laser and LED-based measurement systems. Channel impulse response and path loss were measured and analyzed, providing a benchmark for theoretical and simulation results.

Comparisons between experimental results and analytical models indicate that

the single scattering assumption is adequate for short baseline range and small absorption and scattering coefficients. However, multiple scattering may dominate for large baseline ranges and dense atmosphere conditions. In addition, a gap appeared between measurements and analytical modeling for small pointing angles. The mismatch may be caused by measurement and other system errors, which is still under investigation.

From the link modeling results, the UV communication performance was further predicted and evaluated. We demonstrated that a NLOS UV communication system is typically power limited rather than bandwidth limited even though significant pulse broadening exits after the channel. The thesis also extended the modeling results to account for the scintillation effect for longer ranges. Our case study showed a log-normal distribution for the received signal under turbulence. All of these modeling and analysis results can help to guide the communication system design and development of communication techniques.

Bibliography

[1] R. M. Gagliardi and S. Karp. *Optical Communications*. New York : Wiley, 2nd edition, 1995.

[2] Z. Xu and B. M. Sadler. Ultraviolet communications: Potential and state-of-the-art. *Communications Magazine, IEEE*, 46(5):67–73, May 2008.

[3] D. E. Sunstein. A scatter communications link at ultraviolet frequencies, 1968.

[4] M. R. Luettgen, J. H. Shapiro, and D. M. Reilly. Non-line-of-sight single-scatter propagation model. *J. Opt. Soc. Am. A*, 8(12):1964–1972, 1991.

[5] Z. Xu. Approximate performance analysis of wireless ultraviolet links. In *Proc. of IEEE Intl. Conf. on Acoustics, Speech, and Signal Proc*, Honolulu, Hawaii, April 2007.

[6] S. E. Moran S. Karp, R. M. Gagliardi and L. B. Scotts. *Optical Channels, Fiber, Clouds, Water and Atmosphere*. New York: Plenum, 2nd edition, 1980.

[7] J. R. Kerr, P. J. Titterton, A. R. Kraemer, and C. R. Cooke. Atmospheric optical communications systems. In *Proc. of the IEEE*, volume 58, pages 1691–1709, April 2007.

[8] D. M. Reilly. Atmospheric optical communications in the middle ultraviolet. Master's thesis, Massachusetts Institute of Technilogy, 1976.

[9] X. Zhu, J.M. Kahn, and J. Wang. Markov chain model in maximum-likelihood sequence detection for free-space optical communication through atmospheric turbulence channels. *IEEE Trans. Commun*, 51(3):509–516, 2003.

[10] X. Zhu and J. M. Khan. Free-space optical communication through atmospheric turbulence channels. *Communications, IEEE Transactions on*, 50(8):1293–1300, Aug 2002.

[11] J. M. Kahn and J. B. Barry. Wireless infrared communications. *Proc. IEEE*, 85:265–298, 1997.

[12] A. Tavares, R. Valadas, R. L. Aguiar, and A. O. Duarte. Angle diversity and rate-adaptive transmission for indoor wireless optical communications. *IEEE Commun. Mag*, 41(3):64–73, March 2003.

[13] L. R. Koller. *Ultraviolet Radiation*. John Wiley Sons, New York, 2nd edition, 1965.

[14] Z. Xu, G. Chen, F. Abou-Galala, and M. Leonardi. Experimental performance evaluation of non-line-of-sight ultraviolet communication systems. In *Proc. of the SPIE*, volume 6709, pages 67090Y1–67090Y9, August 2007.

[15] L. B. Stotts and D. D. Bryski. Unattended ground sensor related technologies: an army perspective. In *Proc. of the SPIE*, volume 4743, pages 1–9, 2002.

[16] Iec 60825-12: Safety of laser products - part 12: Safety of free space optical communication systems used for transmission of information, 2005.

[17] D. M. Reilly and C. Warde. Temporal characteristics of single-scatter radiation. *J. Opt. Soc. Am.*, 69(3):464–470, 1979.

[18] D. M. Reilly, D. T. Moriarty, and J. A. Maynard. Unique properties of solar blind ultraviolet communication systems for unattended ground sensor networks. In *Proc. SPIE*, 5611, pages 244–254, 2004.

[19] E. S. Fishburne, M. E. Neer, and G. Sandri. Voice communication via scattered ultraviolet radiation, 1976.

[20] J. J. Puschell and R. Bayse. High data rate ultraviolet communication systems for the tactical battlefield. In *Proc. Tactical Communications Conf*, volume 1, pages 253–267, April 1990.

[21] B. Charles, B. Hughes, A. Erickson, J. Wilkins, and E. Teppo. An ultraviolet laser based communication system for short range tactical applications. In *Proc. of SPIE*, volume 2115, pages 79–86, 1994.

[22] X. Bai, D. Mcintosh, H. Liu, and J. C. Campbell. Ultraviolet single photon detection with geiger-mode 4h-sic avalanche photodiodes. *IEEE Photon. Technol. Lett.*, 19(22):1822–1824, 2007.

[23] S. C. Shen, Y. Zhang, D. Yoo, J. B. Limb, J. H. Ryou, P. D. Yoder, and R. D. Dupuis. Performance of deep ultraviolet gan avalanche photodiodes grown by mocvd. *IEEE Photon. Technol. Lett.*, 19(21):1744–1746, 2007.

[24] G. A. Shaw, M. L. Nischan, M. A. Iyengar, S. Kaushik, and M. K. Griffin. Nlos uv communication for distributed sensor systems. In *Proc. SPIE*, volume 4126, pages 83–96, 2000.

[25] G. A. Shaw, A. M. Siegel, and J. Model. Extending the range and performance of non-line-of-sight ultraviolet communication links. In *Proc. SPIE*, volume 62310C, pages 1–12, 2006.

[26] C. Lavigne, A. Roblin, V. Outters, S. Langlois, T. Girasole, and C. Roze. Comparison of iterative and monte carlo methods for calculation of the aureole about a point source in the earths atmosphere. *Applied Optics*, 38(30):6237–6246, October 1999.

[27] D. Kedar and S. Arnon. Non-line-of-sight optical wireless sensor network operating in multiscattering channel. *Appl. Opt.*, 45(33):8454–8461, 2006.

[28] G. Chen, F. Abou-Galala, Z. Xu, and B. M. Sadler. Experimental evaluation of led-based solar blind nlos communication links. *Opt. Express*, 16(19):15059–15068, 2008.

[29] G. Chen, Z. Xu, and B. M. Sadler. Experimental demonstration of ultraviolet pulse broadening in short-range non-line-of-sight communication channels. *Opt. Express*, 18(10):10500–10509, 2010.

[30] A. Ishimaru. *Wave propagation and scattering in random media*. New York: Academic Press, 1978.

[31] D. M. Junge. Non-line-of-sight electro-optic laser communications in the middle ultraviolet. Master's thesis, Naval Postgraduate School, Monterey, CA, December 1977.

[32] A. S. Zachor. Aureole radiance field about a source in a scattering-absorbing medium. *Applied Optics*, 17(12):1911–1922, June 1978.

[33] J. M. Kahn, W. J. Krause, and J. B. Barry. Experimental characterization of non-directed indoor infrared channels. *IEEE Trans. Commun*, 43:1613–1623, 1995.

[34] M. R. pakravan, M. Kavehrad, and H. Hashemi. Indoor wireless infrared channel characterization by measurements. *IEEE Trans. Vehic. Tech*, 50(4):1053–1073, 2001.

[35] L. R. Bissonnette. Multiscattering model for propagation of narrow light beams in aerosol media. *Applied Optics*, 27(12):2478–2484, June 1988.

[36] G. Chen, Z. Xu, H. Ding, and B. M. Sadler. Path loss modeling and performance trade-off study for short-range non-line-of-sight ultraviolet communications. *Opt. Express*, 17(5):3929–3940, 2009.

[37] Z. Xu, H. Ding, B. M. Sadler, and G. Chen. Analytical performance study of solar blind non-line-of-sight ultraviolet short-range communication links. *Opt. Lett.*, 33(16):1860–1862, 2008.

[38] G. A. Shaw, A. M. Siegel, J. Model, and M. L. Nischan. Field testing and evaluation of a solar-blind uv communication link for unattended ground sensors. In *Proc. SPIE*, volume 5417, pages 250–261, 2004.

[39] H. Ding, G. Chen, A. K. Majumdar, and Z. Xu. A parametric single scattering channel model for non-line-of-sight ultraviolet communications. In *Proc. SPIE*, volume 7091, San Diego, CA, August 2008.

[40] A. K. Majumdar, C. E. Luna, and P. S. Idell. Reconstruction of probability density function of intensity fluctuations relevant to free-space laser communications through atmospheric turbulence. In *Proc. SPIE*, volume 67090M, San Diego, CA, August 2007.

[41] H. Ding, G. Chen, A. Majumdar, B. M. Sadler, and Z. Xu. Modeling of non-line-of-sight ultraviolet scattering channels for communication. *IEEE J. Sel. Areas Commun.*, 27(9):1535–1544, December 2009.

[42] H. Ding, G. Chen, A. Majumdar, B. M. Sadler, and Z. Xu. Modeling of non-line-of-sight ultraviolet scattering channels for communication. *IEEE J. Sel. Areas Commun.*, 29(1):250, January 2011.

[43] C. D. Mobley. *Light and Water: Radiative Transfer in Natural Waters*. Academic Press, 1994.

[44] A. N. Witt. Multiple scattering in reflection nebulae i: A monte carlo approach. *The Astrophysical Journal Supplement Series*, 35:1–6, September 1977.

[45] H. Ding, Z. Xu, and B. M. Sadler. A path loss model for non-line-of-sight ultraviolet multiple scattering channels. *EURASIP: Special Issue on Optical Wireless Communications and Networking*, 2010.

[46] A. K. Majumdar. Laboratory-simulation experiment for optical communication through low-visibility atmosphere using a diode laser. *J. Quantum Electronics*, QE-20(8):919–932, 1984.

[47] Q. He, Z. Xu, and B. M. Sadler. Performance of short-range non-line-of-sight led-based ultraviolet communication receivers. *Opt. Express*, 18(12):12226–12238, 2010.

[48] L. C. Andrews and R. L. Phillips. *Laser Beam Propagation through Random Media*. SPIE Press, 2005.

[49] S. Arnon. Effect of atmosphere turbulence and building sway on optical wireless-communication systems. *Optics Letters*, 28(2):129–131, 2003.

[50] D. L. Hutt and D. H. Tofsted. Effect of atmosphere turbulence on propagation of ultraviolet radiation. *Optical and Laser Technology*, (32):39–48, 2000.

[51] B. Epple. Simplified channel model for simulation of free-space optical communications. *J. Opt. Commun. Netw*, 2(5):293–304, 2010.

[52] R. Otte, L. P. Jong, and A. H. M. Roermund. *Low-Power Wireless Infrared Communications*. Kluwer Academic Publishers, 1999.

[53] M. Razavi and J. H. Shapiro. Wireless optical communications via diversity reception and optical preamplification. In *Proc. ICC*, volume 3, pages 2262–2266, 2003.

[54] G. A. Shaw and M. Nischan. Short-range nlos ultraviolet communication testbed and measurements. In *Proc. SPIE*, volume 4396, pages 31–40, 2001.

[55] G. A. Shaw, A. M. Siegel, and M. L. Nischan. Demonstration system and applications for compact wireless ultraviolet communications. In *Proc. SPIE*, volume 5071, pages 241–252, September 2003.

[56] G. A. Shaw, A. M. Siegel, J. Model, and D. Greisokh. Recent progress in short-range ultraviolet communication. In *Proc. SPIE*, volume 5796, pages 214–225, 2005.